E-16-671

HELICOPTER HOVERING PERFORMANCE STUDIES

I. Vortex Wake Analysis
II. Test Facility
III. Blade Tip Pressure Distributions

FINAL REPORT

R. B. Gray, H. M. McMahon, G. T. Bird,
J. G. Palfery, S. S. Samant, and T. P. Shivananda
School of Aerospace Engineering

October 1976

U.S. Army Research Office
Research Triangle Park, N.C. 27709

Georgia Institute of Technology
Atlanta, Georgia 30332

Grant Nos.
DA-ARO-D-31-124-73-G184
DAAG29-76-G-0007

Disclaimers

The findings in this report are not to be construed as an official Department of the Army position unless so designated by other authorized documents.

Trade names cited in this report do not constitute an official endorsement or approval of the use of such commercial hardware or software.

Disposition Instructions

Destroy this report when no longer needed. Do not return it to the originator.

HELICOPTER HOVERING PERFORMANCE STUDIES

I. Vortex Wake Analysis
II. Test Facility
III. Blade Tip Pressure Distributions

FINAL REPORT

R. B. Gray, H. M. McMahon, G. T. Bird,
J. G. Palfery, S. S. Samant, and T. P. Shivananda
School of Aerospace Engineering

October 1976

U.S. Army Research Office
Research Triangle Park, N.C. 27709

Georgia Institute of Technology
Atlanta, Georgia 30332

Grant Nos.
DA-ARO-D-31-124-73-G184
DAAG29-76-G-0007

REPORT DOCUMENTATION PAGE

READ INSTRUCTIONS BEFORE COMPLETING FORM

1. REPORT NUMBER	2. GOVT ACCESSION NO. / 3. RECIPIENT'S CATALOG NUMBER
4. TITLE (and Subtitle) HELICOPTER HOVERING PERFORMANCE STUDIES I. Vortex Wake Analysis II. Test Facility III. Blade Tip Pressure Distributions	5. TYPE OF REPORT & PERIOD COVERED Final Technical Report Sept. 1, 1973 - Oct. 31, 1976 6. PERFORMING ORG. REPORT NUMBER
7. AUTHOR(s) Robin B. Gray, Howard M. McMahon, George T. Bird, John G. Palfery, Satish S. Samant, and Tumkur P. Shivananda	8. CONTRACT OR GRANT NUMBER(s) DA-ARO-D-31-124-73-G184 DAAG29-76-G-0007
9. PERFORMING ORGANIZATION NAME AND ADDRESS Georgia Institute of Technology School of Aerospace Engineering Atlanta, Georgia 30332	10. PROGRAM ELEMENT, PROJECT, TASK AREA & WORK UNIT NUMBERS 11630-E
11. CONTROLLING OFFICE NAME AND ADDRESS U. S. Army Research Office P. O. Box 12211 Research Triangle Park, North Carolina 27709	12. REPORT DATE October 1976 13. NUMBER OF PAGES 69
14. MONITORING AGENCY NAME & ADDRESS(if different from Controlling Office)	15. SECURITY CLASS. (of this report) Unclassified 15a. DECLASSIFICATION/DOWNGRADING SCHEDULE

16. DISTRIBUTION STATEMENT (of this Report)

This document has been approved for public release and sale; its distribution is unlimited.

17. DISTRIBUTION STATEMENT (of the abstract entered in Block 20, if different from Report)

18. SUPPLEMENTARY NOTES

19. KEY WORDS (Continue on reverse side if necessary and identify by block number)

Blade tips	Pressure distributions	Rotary wings	Wing tips
Helicopters	Pressure measurements	Test facilities	
Helicopter Performance	Rotor aerodynamics	Test stands	
Helicopter Wakes	Rotor blades	Vortices	
Lifting Rotors	Rotor lift	Vorticity	

20. ABSTRACT (Continue on reverse side if necessary and identify by block number)

Results are presented from studies of several problem areas which are related to helicopter hovering performance prediction. A working hypothesis is described for including the tip vortex core effect in a vortex wake analysis and it is shown that the tip vortex geometry in the near wake can be calculated with good accuracy for rotors having fewer than five blades. A hovering model rotor test facility of reduced size is described. Data from this facility include measured pressure distributions on the tip of a single-bladed rotor.

SUMMARY

Results are presented from several studies included in a research program whose overall objective is to improve the reliability of analytical methods for predicting helicopter hovering performance. These studies are in the areas of vortex wake analysis, model test facility development, and tip effects.

In the vortex wake analysis, a term is introduced to represent a simple model of the tip vortex core effect. The results show that with this effect included, the tip vortex geometry in the near wake can be calculated with much better accuracy for one-, two-, three-, and four-bladed rotors than has been possible to date.

A hovering model rotor test facility of reduced size when compared with the large room concept has been developed. The facility provides acceptable isolation for the rotor and improved protection for personnel and equipment.

Measurements of absolute pressure distributions on the tip of a single-bladed model rotor have been obtained. The constant chord, untwisted blade has a square tip and an NACA 0012 airfoil section. Data are presented for thrust coefficients of 0, 0.0026, and 0.0055 at tip Reynolds numbers of approximately 540,000 and 740,000.

FOREWORD

The work described herein is part of an ongoing research program directed toward improving the reliability of analytical methods for predicting helicopter performance. The primary effort has been devoted to developing a more accurate method for calculating the tip vortex geometry for use in vortex wake analyses and a model test facility to provide data for comparison with theoretical results. In this latter regard, absolute pressure distributions have been measured on the tip of a model rotor blade. These data will be useful in validating lifting surface theories and as documentation for three-dimensional tip effects.

The work was performed for the U.S. Army Research Office, Research Triangle Park, North Carolina, as Project No. 11630-E under Grant Nos. DA-ARO-D-31-124-73-G184 and DAAG29-76-G-0007 by the School of Aerospace Engineering, Georgia Institute of Technology, Atlanta, Georgia. The Technical Monitors were Mr. James J. Murray, Director, Engineering Sciences Division, and Dr. Robert E. Singleton, Chief, Fluid Mechanics Branch, Engineering Sciences Division. The Co-Principal Investigators were Regents' Professor R. B. Gray and Professor H. M. McMahon.

The results for the vortex wake analysis are taken from the Ph.D. dissertation of Satish S. Samant.

The model hovering test facility was under development for a number of years. Its design was based on extensive tests of a one-quarter scale prototype in which model airplane propellers were used. The basic facility configuration was determined by D. W. Logan and K. F. Schrantz, Jr. and it was their success that led to the construction of the present installation. Additional work on the prototype was performed by O. L. Ernest and D. R. Parker. Preliminary investigations of some of the instrumentation including the development of calibration and test techniques were conducted by S. J. Helf and S. Lakshminarayan. All of those named were graduate students and have earned the Master of Science degree.

The design of the test facility was the responsibility of G. T. Bird, Research Engineer, who also supervised the construction and assembly phase. The design of the model rotor and data acquisition system, the incorporation of the instrumentation, and the development of the computer software were the responsibility of J. G. Palfery, Research Engineer. Both of these engineers gave valuable assistance in the development of calibration and operating procedures and in conducting the initial tests.

The preliminary determination of the rotor drag tares and tests of the flush-mounted pressure transducer were accomplished by M. S. Mathews and R. V. Kennedy respectively. Qualitative flow visualization studies of the flow in the test cell were performed by G. T. Downs. Mr. S. Peters conducted calibration tests of the vector anemometer while B. Platt assisted with the instrumentation installation and circuitry. The

compilation of two-dimensional airfoil characteristics versus Reynolds number for use in the model performance analysis was done by D. P. Schrage. Mr. R. K. Shenoy assisted with extensive tests to determine the model tares and performance characteristics, with flow visualization studies, and with the data analysis. Mr. T. P. Shivananda also assisted with these activities and, in addition, calibrated the pressure transducers and the vector anemometer and developed the necessary computer software. All of these graduate students have also earned the Master of Science degree.

The pressure distributions on the blade tip are from the Ph.D. dissertation of T. P. Shivananda. Professor J. I. Craig provided valuable advice during the development of the data-acquisition software for the computer. J. Caudell, Research Associate, organized and installed the instrumentation that was used in the test program.

The construction of the model rotor and its supporting and drive mechanisms was performed by H. W. Meyer, D. L. Ransom, and C. F. Wiser.

TABLE OF CONTENTS

LIST OF ILLUSTRATIONS

LIST OF TABLES

I. VORTEX WAKE ANALYSIS

INTRODUCTION

A brief discussion of the state-of-the-art of hovering helicopter analyses is given below. Its purpose is to point out some of the inherent limitations and some of the areas where improvement is needed. In particular, attention is directed to the problem of determining the local blade section angle of attack which, in accordance with Prandtl's hypothesis, is directly related to the local relative velocity vector. An excellent survey and a comprehensive bibliography of the field is given in Ref. 1. One of the conclusions of that paper is that the determination of the local relative velocity vector is very sensitive to the position of the tip vortex relative to the blade. The effort reported on herein is directed toward improving the analytical methods for determining this location of the tip vortex.

Historically, the results that have been obtained from the simplified performance analyses for hovering rotors have been remarkably good considering the simplifications that were introduced in attempting to model the very complicated flow field. These early simple theories as well as those that represent the current state-of-the-art are based on blade element theory. This approach neglects any spanwise flow and assumes that the blade element develops forces and moments consistent with those of the two-dimensional airfoil operating at the same effective angle of attack and relative velocity. The neglect of the spanwise flow is reasonable relative to the effects of other simplifications. The use of coefficients from two-dimensional airfoil tests permits approximate allowances for scale, compressibility, and stall effects. However, their use does introduce empiricisms into the analysis.

The primary defect in rigid-blade aerodynamic analyses is due to the methods employed for determining the effective angle of attack of each blade element. In principle, all of the methods replace the blade with its equivalent lifting line. The relative velocity vectors normal to and at points along the lifting line are determined by one of several methods to be discussed. These vectors and the local blade pitch angles then give the angle of attack of the local blade elements.

The earlier analyses used simple momentum theory which yields a constant induced velocity over the rotor disc. Later analyses used an annular momentum theory which is analogous to the simple momentum theory and yields a variable induced velocity over the disc. These induced velocities when added vectorially to the product of the blade angular velocity and the blade-element radius yield the local relative velocity vector. The relationship of this vector with the zero lift line of the blade element gives the local angle of attack. Since lift and drag coefficients are directly related to the angle of attack, one could, at this stage, select these coefficients from the results of two-dimensional tests of the airfoil section and calculate the spanwise aerodynamic

loading. If these coefficients are used, the loading will not compare well with experimental loadings due to the simplifications introduced in determining the induced velocities and hence the angles of attack. The approach, then, has been to use mean values for the section parameters as determined from tests of geometrically similar rotors. Although the spanwise load distribution is still not correct, the integrated values of the thrust and power become acceptable for performance evaluations and for comparisons between rotors of similar design. However, the results obtained may be in considerable error when the method is applied by extrapolation to rotors of different geometry. The problem here is that the degree of interaction of the blades with the trailing vortex system changes as the number of blades changes. The momentum methods cannot account for this effect. As far as tip loss is concerned, it may be approximately accounted for by introducing an effective radius.

The Goldstein-Lock method (Ref. 2) was an improvement in that tip loss and the effect of blade number were better represented. However, this method was developed for propellers in axial flight and was based on an optimum propeller analysis whose vortex wake did not include a strong tip vortex. Strictly speaking, this method is not applicable to the static thrust case but it has been used with good results. Its deficiency has been that it becomes increasingly optimistic for hovering rotors as the number of blades increases. This is primarily due to its inability to assess the degree of interference between a tip vortex and the following blades.

Landgrebe (Ref. 3) presents a prescribed vortex wake analysis. This approach requires the experimental determination of the tip vortex geometry as a function of blade number, blade twist, and thrust coefficient. Given this geometry, the induced velocity can be calculated along the lifting line representing the blade using the Biot-Savart equation and the aerodynamic loadings can be determined in the same manner as for the simple blade element theory. The appropriate airfoil section characteristics are those of the two-dimensional airfoil tested at the same effective angle of attack, Reynolds number, and Mach number. The resulting blade loadings, thrust, and power agree well with experiment. A tip loss effect is obtained by fairing the thrust loading distribution curves to zero at the blade tip.

A satisfactory method for theoretically determining the tip vortex geometry has not been published. This paper describes a working hypothesis and gives several examples of its application to the determination of tip vortex geometries. Although significant improvements are shown, further refinement is required. For example, the solid-body rotation model of the tip vortex core is not completely satisfactory for determining the motion and geometry of the tip vortex. It is concluded that an appropriate model of the tip vortex core structure is all that remains to be deterimined to place the vortex wake analysis on a completely theoretical basis for those cases in which the lifting line approximation is applicable.

DISCUSSION OF PROBLEM

References 1, 3, 4, and 5 discuss, among other topics, the application of the vortex wake methods to the prediction of helicopter hovering performance and to the calculation of the flow field about hovering rotors. References 1, 3, and 5 illustrate the sensitivity of the results to the location of the tip vortex. References 3 and 4 present examples of the results of theoretical analyses for calculating the tip vortex geometry. In general, these results exhibit axial displacement velocities and rates of contraction of the tip vortex which are too small relative to the measured values. Consequently, empirical analyses which are based on measured parameters have been developed. Examples of these analyses are given in Refs. 3, 6, 7, and 8.

The theoretical analyses are based on the Biot-Savart law which relates the velocity field of a vortex to its strength and geometry. The approach is to select an initial geometry, to calculate the induced velocity vector along the centerline of the vortex, and then to numerically allow the initial geometry to deform for a short period of time under the influence of the calculated flow field to a new geometry. The process is repeated until the changes in geometry from one step to the next are acceptably small. This procedure has been applied to several cases in which the initial geometry was selected using measured parameters from Refs. 3 and 6. The results are shown in Fig. 1 for one- and two-bladed rotors and compare well with the theoretically calculated geometry of Refs. 3 and 4 but do not compare well with the measured geometry. The conclusion is that significant contributing factors are omitted or are not properly modeled in the analysis.

Several possibilities have been investigated and their effect on the tip vortex geometry has been assessed approximately:

1. A model in which part of the inner sheet rolls up with the tip vortex thereby reducing the strength of the tip vortex as it moves down the wake. Computer studies showed that this may occur, reducing the tip vortex strength by about ten per cent during the first revolution of the blade for single-bladed rotors.

2. A wake model of finite length whose boundaries contract and then expand. This model was based on qualitative flow visualization studies of a model propeller.

3. An approximate lifting surface model.

The effect of each of these on the calculated tip vortex geometry for a single-bladed rotor was small, giving slightly better agreement in some cases and poorer agreement in others. Since a lifting line representation of the rotor with a prescribed wake geometry has been shown to give good performance results (Ref. 3), it was concluded after

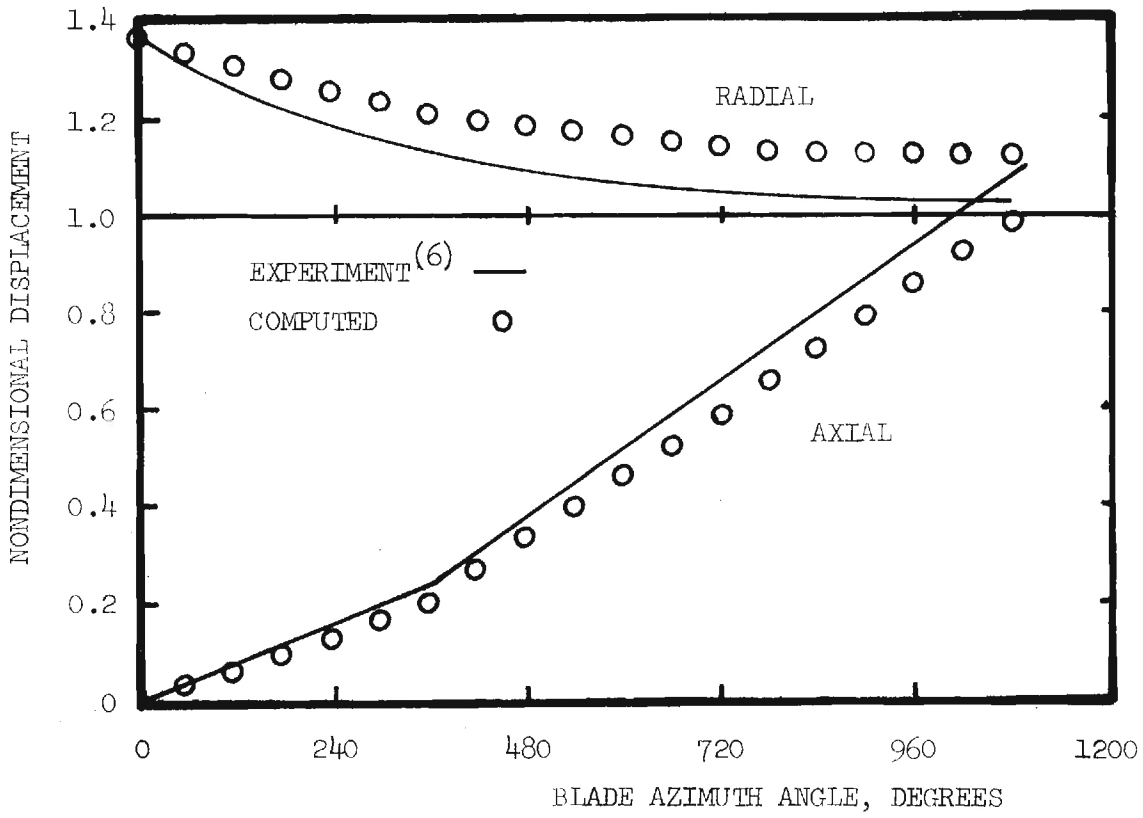

a) Single-bladed rotor, $C_T = 0.00280$, $\sigma = 0.040$

Figure 1. Typical comparison between measured and computed tip vortex geometry without correction for vortex core effect.

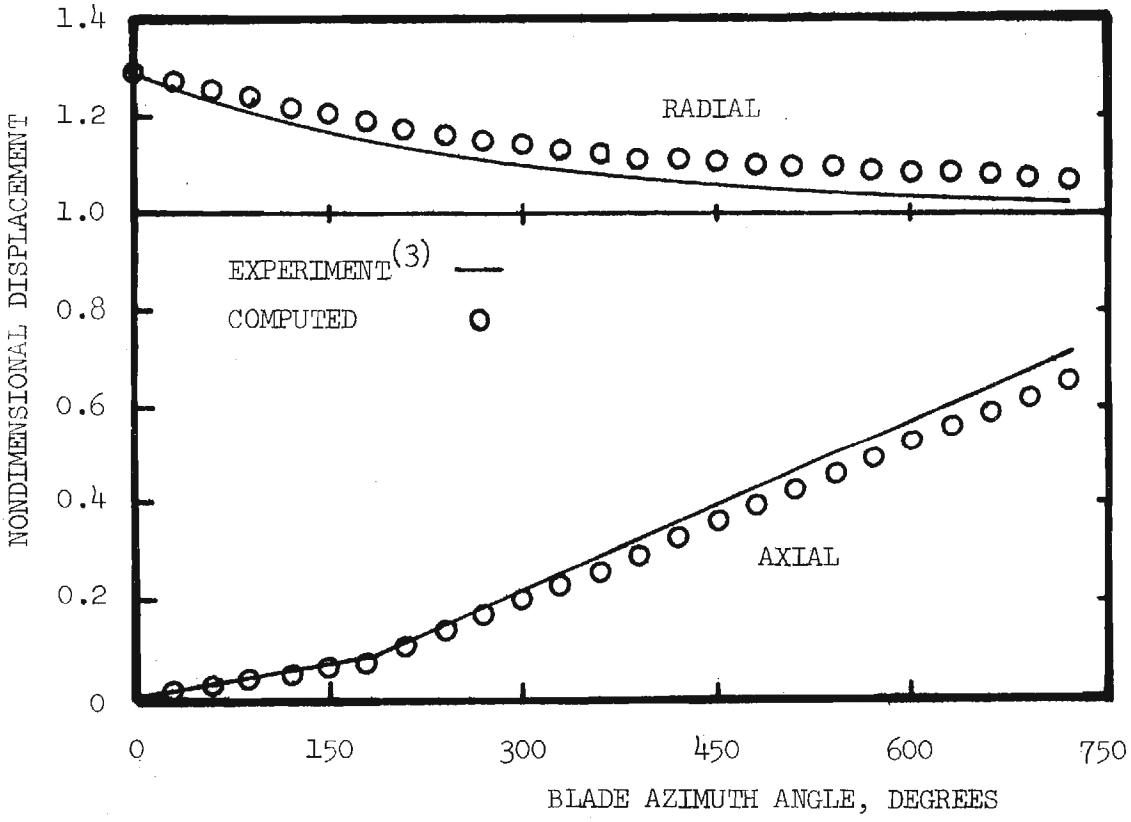

b) Two-bladed rotor. $C_T = 0.00283$, $\sigma = 0.070$

Figure 1. Concluded.

a reassessment of the problem that a major part of the discrepancies observed in Fig. 1 could possibly be due to the lack of a proper model of the tip vortex core structure.

With this in mind, further consideration was given to the experimental methods used to obtain the geometric parameters presented in Refs. 3, 6, 7, and 8. All of these measurements were made in a radial plane in which the motion of the tip vortex was traced as a function of blade angular displacement relative to the plane. As a result, the velocities that would then be measured are the apparent velocities in the radial and axial directions only. The angular velocity or motion of the vortex element out of the plane can not be perceived. If an angular velocity exists, then the identity of the vortex element being observed in the plane changes with time and thus with the blade angular displacement. The displacement of the tip vortex in the plane is then also an apparent displacement. This does not create any problems in the prescribed wake analysis. The measured geometry is, of course, correct and the application of the Biot-Savart law to the tip vortex with any reasonable core model will yield acceptable values of the induced velocity except in the immediate vicinity of the vortex and within its core.

However, when the Biot-Savart law is used in a theoretical analysis to calculate the tip vortex geometry, the true velocity components for vortex elements of fixed identity must be determined. The geometry is found by allowing these elements of fixed identity to displace in the three coordinate directions. The procedure is iterative in nature and the solution is assumed to be reached when the geometry no longer changes with time. The problem, as noted before, is that the converged solution does not compare well with that measured, particularly in the near wake.

In calculating the velocity components associated with the entire vortex system for an element of fixed identity, other elements of the system at a distance from the element under consideration can be treated as line elements. However, the contributions of the element itself and of adjacent elements are highly dependent on the size and structure of the vortex core. The core model that has been generally used in the past is one having solid body rotation. This model does not appear to be entirely correct and this may be the primary source of the discrepancies that are observed in Fig. 1.

The possibility of developing a physically accurate model did not appear to be feasible. Little information of a specific and finely detailed nature is available in the literature although promising work is being done using laser velocimeters. From what is known, it would seem that the core model should qualitatively be composed of vortex filaments wrapped in a spiral fashion about a contracting helical line. There may be both positive and negative vorticity and this vorticity of opposing signs may form a number of alternating layers not necessarily concentric with the helical line. In any event and due to the curva-

ture of the helical line, the vorticity distribution within the core will not be symmetric with respect to the line. The mathematical modeling and analysis of such a system will certainly be complex and, depending upon the simplifications introduced, will probably be at least as time consuming on a computer as the current vortex wake analyses themselves.

If it is assumed that a physically accurate core model is available, one may then consider how it could be used in the determination of the tip vortex geometry and what steps might be taken to reduce the computer time required. For example: The effect of the core should be very localized since the ratio of the core diameter to the rotor diameter is small. Then for points not near the core, the tip vortex can be treated as a line vortex. As noted before, this accounts for the success of the prescribed vortex wake analyses. In addition, since the core diameter is small and the tip vortex is curved, only small elements of arc length may need to be considered on either side of the point on the tip vortex where the displacement velocities are to be calculated. The remainder of the vortex system may then be treated as line vortices. Further, it may turn out after investigation that the solid-body core model (or similar simple model) is adequate for calculating the axial components of the core effect so that the more complicated model may only need to be used for calculating the radial and tangential components. In the former case, the situation may be more clear-cut and hence simpler in concept if a vortex tube is postulated. Then a bounding surface for the vortex is defined and an average axial velocity component can be determined for points on this surface. For the latter case, however, the situation is different. The vorticity distribution within the tube has associated with it a velocity distribution. Each layer of vorticity then has a different component in the radial and tangential directions and the question arises as to what basis should be used to determine a mean radial and tangential velocity for the vortex tube as a whole.

The preceding discussion suggested an approach which was capable of being tested. Initially, it was planned to select several prescribed vortex wake models, to use the theoretical procedure of Ref. 4 to calculate the induced velocity components along the tip vortex, and then to calculate only the tangential velocity component (attributable to the core effect) that is required to prevent the prescribed geometry from deforming. This approach proved to be unproductive but it did set the stage for further development of the analysis.

ANALYSIS

The wake model is similar to that of Ref. 4. The blades are replaced by their equivalent lifting lines. A rolled-up vortex having a finite core diameter is shed from the tip of each blade. The sheet that is shed from the blade trailing edge inboard of the point of maximum bound vortex strength is approximated by a number of finite strength vortex filaments. The strength of each of these filaments is

equal to the change in bound vortex strength over the spanwise interval of the sheet element that is replaced by the filament. Each of these filaments lies on a contracting circular cylindrical surface whose local radius is equal to the corresponding local radius of the tip vortex times the non-dimensional radius of the blade at which the filament was shed. The axial position of each filament is approximated by integrating the velocity history of the outermost filament and specifying that the axial position of each filament is determined by the product of the position of the outermost filament and the ratio of the local radial position of each filament to that of the outermost filament. This method of locating the inner wake filaments appears to be a reasonable approximation and represents a trade-off of some accuracy for a considerable amount of computing time. The medium is a perfect fluid. Therefore, by suppressing any instabilities of physical or numerical origin, an ultimate wake exists. This ultimate wake is, by definition, a region in which no further deformation of the vortex system occurs. It is implied in this latter statement that the inner sheets, due to their outer filaments having a higher axial velocity and their inner filaments having a lower axial velocity than the tip vortex system, have coalesced to form a volume distribution of vorticity. Then as far as the tip vortex system is concerned in the ultimate wake, the inner sheets appear to be a concentrated line vortex located on the wake axis and having a strength equal to the sum of the strengths of the tip vortices.

It is noted that it is immaterial to the physical system whether or not an ultimate wake is assumed to exist in the theoretical model. Such an ultimate wake is at so great a distance from the rotor plane and the near wake where the flow field is to be calculated that its influence through the Biot-Savart law is negligible. The important criteria is that the physical wake exhibit a tendency to approach the ultimate wake configuration within a diameter or so of the rotor plane. A second observation is that the action of viscosity in spreading and finally breaking up the wake may be neglected if this effect proceeds at a much slower rate than that at which the vortex system moves down the wake. The primary reason for introducing the ultimate wake concept is that it permits the determination of a relationship which is important in the development of the analysis.

The analysis of Ref. 4 is particularly well suited for this problem because the determination of the tip vortex geometry is developed in terms of the apparent induced velocity components. In order to apply that analysis to calculating the tangential velocity attributable to the core effect, several expressions must be modified to include this effect. These expressions are redeveloped below to illustrate the modifications.

The analysis uses the Biot-Savart law to determine the induced velocity components associated with the entire vortex system, but excluding the core effect, at selected points along the tip vortex. The resulting equations (Ref. 4) include terms involving the radial and

axial pitch angles of the tip vortex. These angles are defined in a coordinate system that is rotating with the blade since the flow field is steady with respect to this system. In addition, they are defined in terms of the velocity components of a vortex element of fixed identity which is moving in this system. These velocity components have contributions from the vortex system as computed using the Biot-Savart law, the blade rotational velocity, and from what has been termed the core effect. If it is hypothesized that the contribution of the core effect to the radial and axial velocities is adequately obtained from the solid-body rotation model, then the method given in Ref. 4 is applicable and the only contribution that is undefined is the contribution to the tangential component.

The relevant velocity diagrams with respect to the blade for a point in the near wake are shown in Fig. 2. The expressions for the pitch angles in terms of the true velocity components and then the apparent velocity components are

$$\text{TAN } \varphi_p = \frac{w'_p}{\Omega r_p + v'_c + v'_p} = \frac{w'_{a_p}}{\Omega r_p} \tag{1a}$$

and

$$\text{TAN } \beta_p = \frac{u'_p}{\Omega r_p + v'_c + v'_p} = \frac{u'_{a_p}}{\Omega r_p} \tag{1b}$$

where u'_p, v'_p, and w'_p are the radial, tangential, and axial induced velocity components that are associated with the entire vortex system, except that the core effect in the tangential component is expressed separately as v'_c; u'_{a_p} and w'_{a_p} are the radial and axial apparent velocity components; and Ωr_p is the velocity relative to the rotating blade of a fixed-in-space point that corresponds to the point moving with the tip vortex.

With these modified equations and starting with a prescribed wake model, the analysis of Ref. 4 can be used to calculate the required value of v'_c which will maintain the initial geometry. As noted before, this was unproductive since Eqs. (1a) and (1b) gave different values of v'_c. While it might be expected that the core effect would be different in the two orthogonal directions, logic and model consistency exclude two different core corrections for the tangential velocity. However, the calculations did lead to the discovery of two mathematically simple corrections which prevented the initial vortex geometry from deforming. Then after further consideration, approximate forms of Eqs. (1a) and (1b) were found that are consistent.

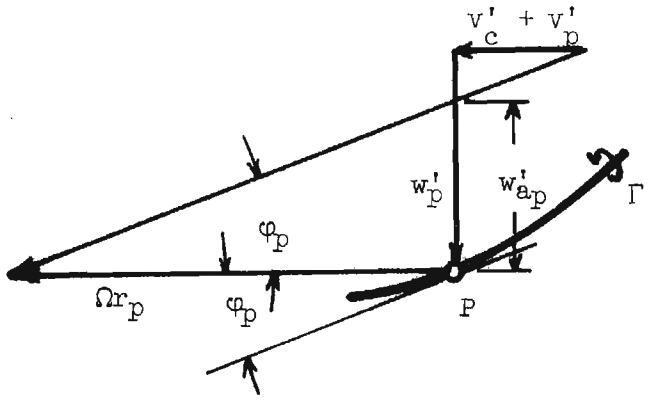

a) Axial pitch angle and apparent axial induced velocity component.

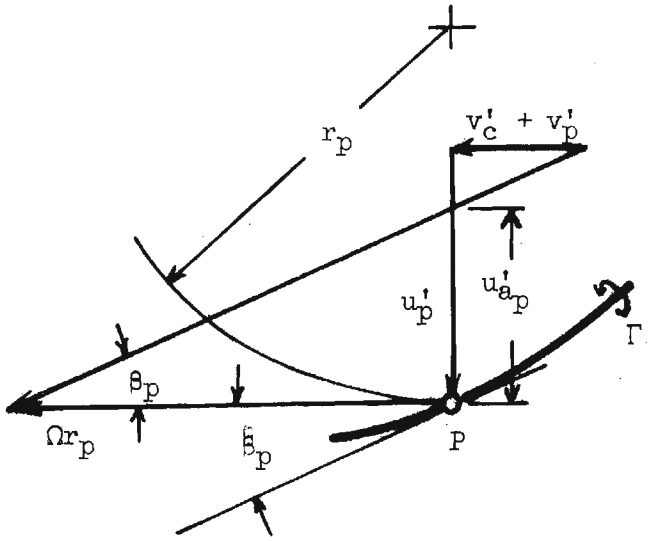

b) Radial pitch angle and apparent radial induced velocity component.

Figure 2. Velocity diagrams for determining the tip vortex pitch angles and apparent induced velocity components for points on the tip vortex in the near wake.

The approximate expressions are more conveniently developed in a nondimensional form in which the velocity terms are normalized by the product ΩRAC_Γ and the lengths by RA which is the ultimate wake radius of the tip vortex. The normalized forms of Eqs. (1a) and (1b) are then

$$\text{TAN } \varphi_p = \frac{w_p}{\left(\frac{\Omega r_p + v_c'}{\Omega RAC_\Gamma}\right) + v_p} = \frac{w_{a_p}}{x_p}\frac{C_\Gamma}{} \tag{2a}$$

$$\text{TAN } \beta_p = \frac{u_p}{\left(\frac{\Omega r_p + v_c'}{\Omega RAC_\Gamma}\right) + v_p} = \frac{u_{a_p}}{x_p}\frac{C_\Gamma}{} \tag{2b}$$

It was discovered that if the sum $(\Omega r_p + v_c')/\Omega RAC_\Gamma$ were replaced by the term Jx^i/C_Γ where J is a parameter which forces the tip vortex strength to be equal to the maximum blade bound vortex strength, then the distortion of the tip vortex from the initial prescribed geometry would be small. With this substitution, Eqs. (2a) and (2b) become

$$\text{TAN } \varphi_p = \frac{w_p}{\frac{Jx_p^i}{C_\Gamma} + v_p} = \frac{w_{a_p}}{x_p}\frac{C_\Gamma}{}, \tag{3a}$$

$$\text{TAN } \beta_p = \frac{u_p}{\frac{Jx_p^i}{C_\Gamma} + v_p} = \frac{u_{a_p}}{x_p}\frac{C_\Gamma}{}. \tag{3b}$$

In the ultimate wake, $x = 1$ and Eq. (3a) can be solved for J so that

$$J = \frac{w_\infty}{\text{TAN } \varphi_\infty}\frac{C_\Gamma}{} - C_\Gamma v_\infty \tag{4}$$

where C_T is the maximum blade bound vortex strength coefficient and therefore, by assumption, the tip vortex strength coefficient. The determination of J requires an iterative process in which the method of Ref. 4 is used to calculate the bound vortex strength distribution near the blade tip to determine its maximum. The procedure begins with $J = 1$ and proceeds until the change in J between successive iterations becomes acceptably small.

Equations (3) represent three different cases that have been explored. If $J = 1$ and $i = 1$, then the equations are identical with those of Ref. 4 and the results are shown in Fig. 1. If $i = 0$, good agreement is obtained with the measured axial displacements as will be shown later. If $i = -1$, then good agreement is obtained with the measured radial displacements as will also be shown later. It is seen that for the latter two values of i, the value of the denominators of the two middle expressions in Eqs. (3a) and (3b) are identical for points in the ultimate wake where $x_p = 1$. However, they are different for points in the near wake. This, of course, represents an inconsistency as noted before. The question, then, is: why does the procedure result in such good agreement with the measured geometry? A plausible answer which leads to a working hypothesis is given below.

If i is set equal to zero in Eq. (3a) and equal to minus one in Eq. (3b) and if the right-hand equalities are then solved for the apparent induced velocity components, the resulting equations are:

$$w_{a_p} = \frac{w_p}{\frac{J}{x_p} + v_p \frac{C_T}{x_p}} \tag{5a}$$

and

$$u_{a_p} = \frac{u_p}{\frac{J}{x_p^2} + v_p \frac{C_T}{x_p}} \quad . \tag{5b}$$

Again note that the denominators of these expressions are different when x_p is not equal to one.

Computations show that the second term in the denominator of Eqs. (5) is, in general, at least two orders of magnitude smaller than the first term and may therefore be neglected with negligible error in comparison with the experimental errors inherent in the measured geometry. Then,

$$w_{a_p} \approx \frac{w_p}{J/x_p} \quad . \tag{6a}$$

$$u_{a_p} \approx \frac{u_p}{J/x_p^2} = \frac{u_p x_p}{J/x_p} \quad . \tag{6b}$$

The denominators of Eqs. (6) are now equal and the previous inconsistency in this respect has been eliminated. In addition, and based on this result, the core correction to the tangential induced velocity component is

$$v_c = \left(\frac{J}{x_p} - 1\right) \frac{x_p}{C_\Gamma} \quad . \tag{7}$$

In general, J/x_p is less than unity in the near wake so that a core element of fixed identity has an additional tangential component in the direction of blade rotation than it would otherwise have. This is qualitatively consistent with the results of flow visualization studies.

Considering next the numerator product, $u_p x_p$, of Eq. (6b), the results of flow visualization studies show that the radius of the contracting wake may be approximated with good accuracy, according to Ref. 6, by

$$x_p = \frac{r_p}{RA} = 1 + \frac{C}{A} e^{-\lambda\Psi} \tag{8}$$

where A, C, and λ are experimentally determined parameters which depend upon the rotor geometry and thrust. Substituting this expression into Eq. (6b) gives the core correction to the radial induced velocity as

$$u_c = u_p \frac{C}{A} e^{-\lambda\Psi} \tag{9}$$

This again is qualitatively consistent since u_c approaches zero in the ultimate wake as does u_p and the exponential factor.

With regard to the core effect in the axial component of the induced velocity, the method of Ref. 4 which uses the solid-core model appears to give an acceptable value in that the calculated geometry has a good agreement with that measured. The contributions from this core model to the other two components are small and can properly be neglected at this stage.

Although the foregoing semi-empirical analysis produces improved agreement between computed and measured tip vortex geometries when the initial geometry is prescribed, it has not been used in a completely theoretical computation. A preliminary attempt has been tried and problems have arisen. It is not known at this time whether or not these problems can be resolved. Eqs. (7) and (9) suggest simplified models of the vortex core structure but these are also untried at this time.

RESULTS

The preceding results have been incorporated into an analysis similar to that of Ref. 4 except that initial prescribed tip vortex wake geometries were chosen for a range of blade numbers and thrust coefficients. The purpose was to determine if the subsequent computations maintain the initially selected geometry without the appearance of deformations. The first trial calculation involved the use of Eqs. (3) and (4) for $i = 0$. The results are shown in Fig. 3 for a one- and a two-bladed rotor. The solid lines represent the faired experimental data from Refs. 6 and 3 respectively and also the initial tip vortex geometry used to begin the analysis. The points show the calculated locations of the vortex elements after several iterations. The agreement in the axial position is very good and a comparison with Fig. 1 shows that the agreement in the radial position is improved. The second trial calculation was for the same cases but for $i = -1$. These results are shown in Fig. 4. Here, the agreement in the radial position is very good and a comparison with Fig. 1 shows that the agreement in the axial position is equally as poor but the error is in the opposite direction.

In proceeding to other trial calculations involving rotors developing different thrust levels and having different numbers of blades, the approach was changed somewhat so that, effectively, Eqs. (4) and (6) were used. The cases covered, including those previously discussed, are listed in Table 1 which gives the blade number, the thrust coefficient, the blade pitch angle, the measured parameters for the tip vortex geometry, and the calculated value of J. The data, except for J, were obtained from Refs. 6 and 7 for the one-bladed rotor, Ref. 3 for the two-bladed rotor, and Ref. 8 for the three- and four-bladed rotors. The calculated results are compared with the measured data in Figs. 5 through 11. The agreement is equally as good as for those cases previously discussed except at the highest thrust levels. The reason for the observed deviation between measured and calculated geometries

Table 1. Geometric Data and Calculated Values of J for the Cases of Rotors Considered

Fig.	b	C_T	σ	θ	A	λ	K_1	K_2	J	Ref.
5	1	.00195	0.040	6.5°	.746	.160	.0218	.0420	1.15	6
1,3,4	1	.00280	0.040	8.5°	.733	.164	.0280	.0490	1.15	6
6	1	.00370	0.040	10.1°	.722	.177	.0338	.0569	1.11	6
7	2	.00193	0.070	6.0°	.780	.197	.0138	.0439	1.05	3
1,3,4	2	.00280	0.070	8.0°	.780	.221	.0200	.0529	.95	3
8	2	.0035	0.070	10.1°	.780	.239	.0250	.0592	.96	3
9	3	.00220	0.105	6.0°	.780	.190	.0150	.0470	1.36	8
10	3	.00320	0.105	8.0°	.780	.225	.0191	.0560	1.22	8
11	4	.00371	0.140	8.0°	.780	.245	.021	.06	1.45	8

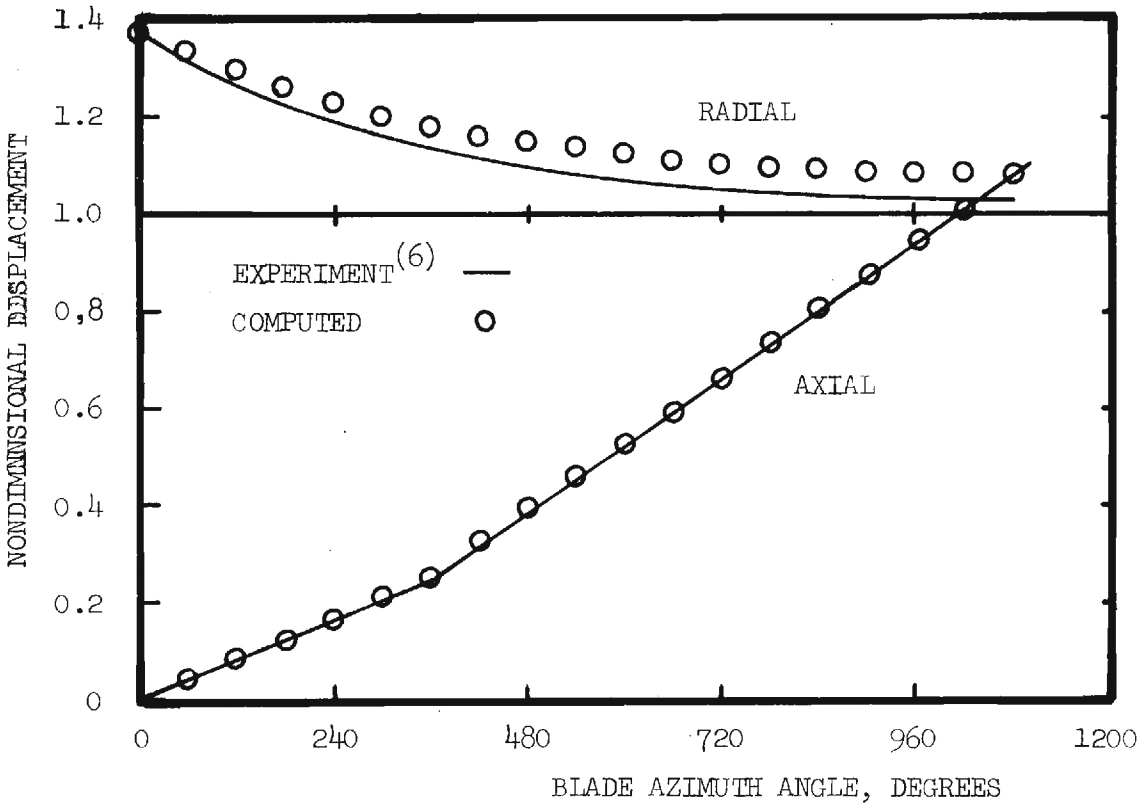

a) Single-bladed rotor, $C_T = 0.00280$, $\sigma = 0.040$

Figure 3. Comparison between measured and computed tip vortex geometry with correction for vortex core effect in axial displacement.

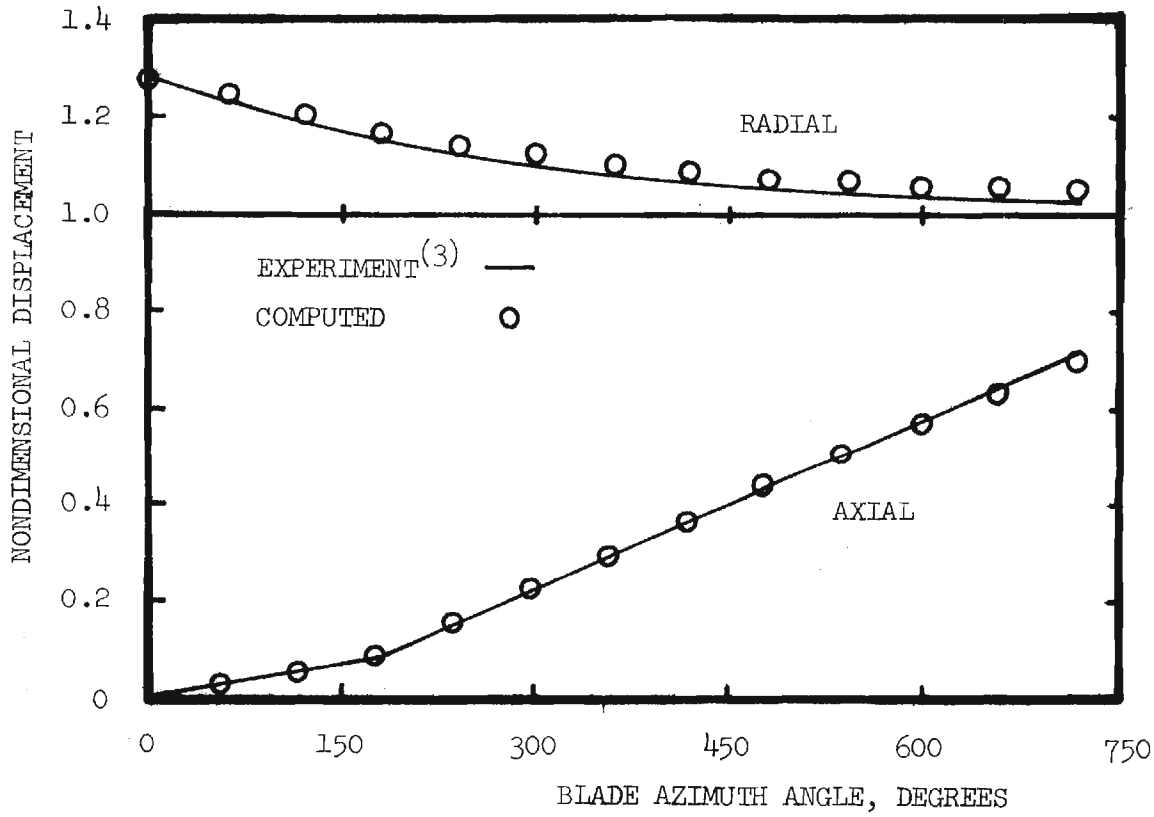

b) Two-bladed rotor, $C_T = 0.00283$, $\sigma = 0.070$

Figure 3. Concluded.

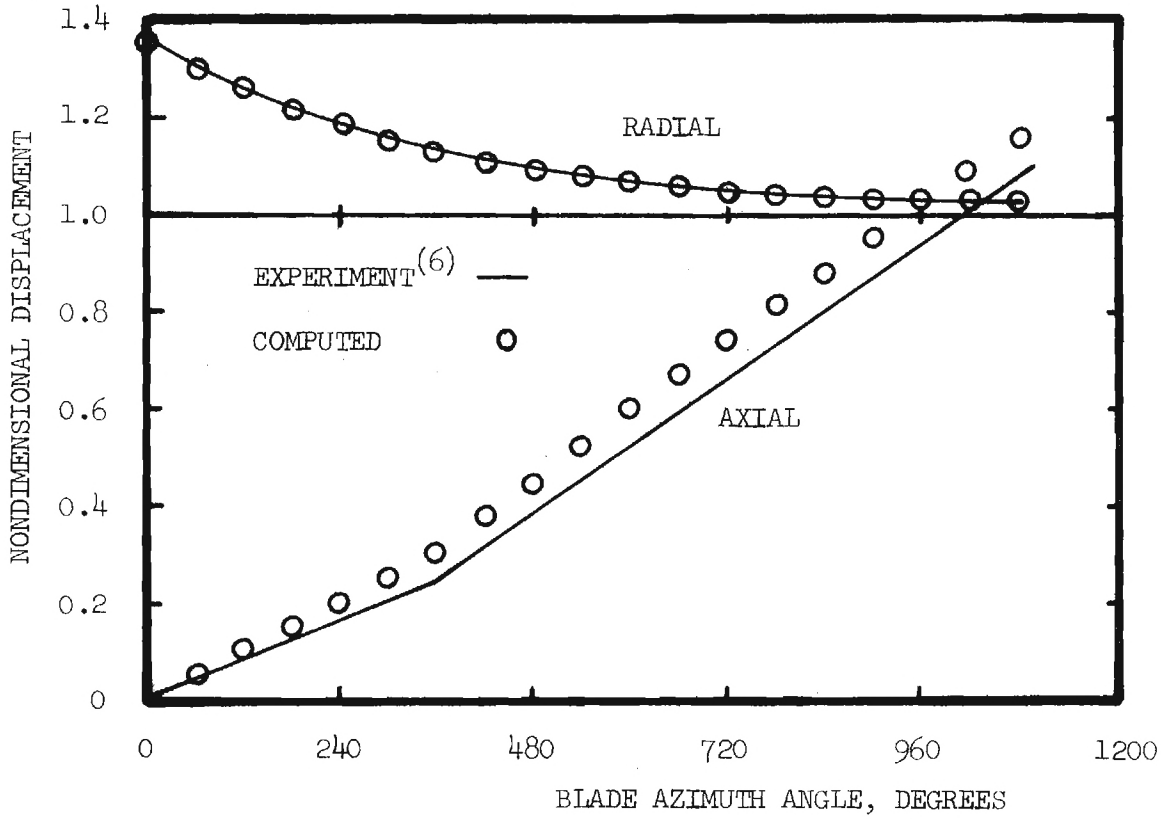

a) Single-bladed rotor, $C_T = 0.00280$, $\sigma = 0.040$

Figure 4. Comparison between measured and computed tip vortex geometry with correction for vortex core effect in radial displacement.

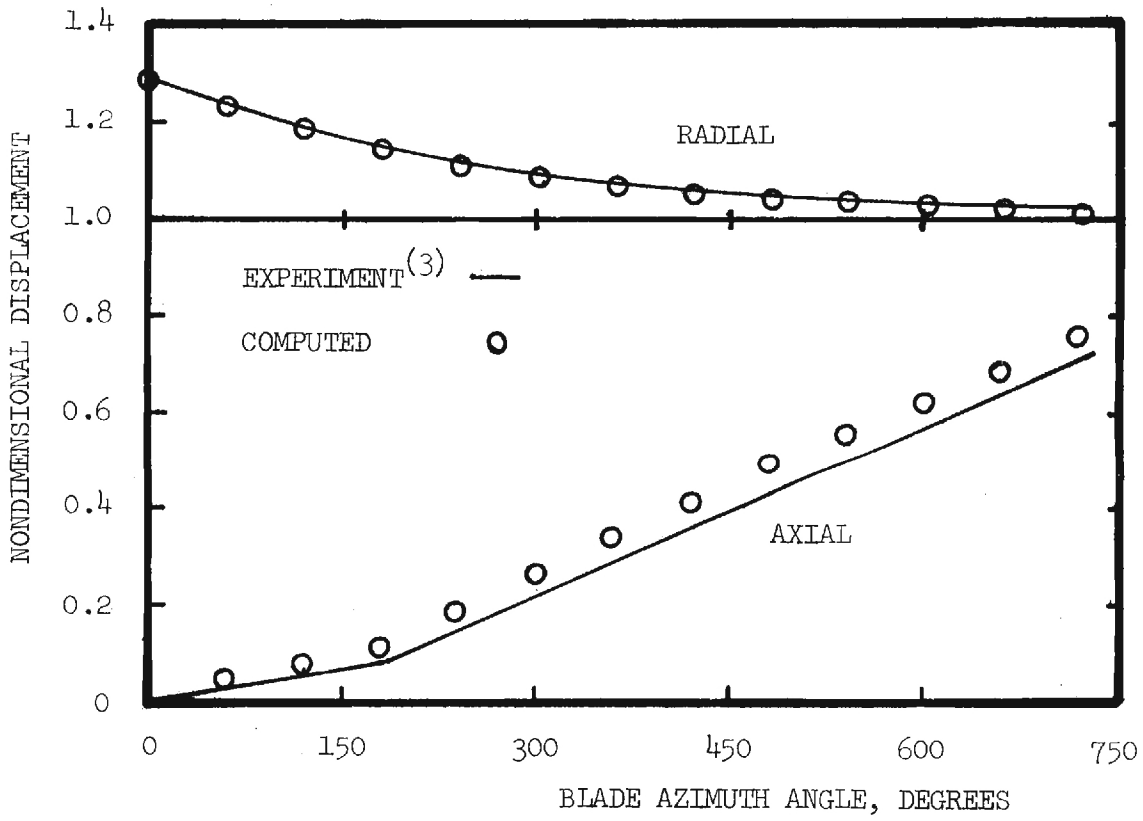

b) Two-bladed rotor, $C_T = 0.00283$, $\sigma = 0.070$

Figure 4. Concluded.

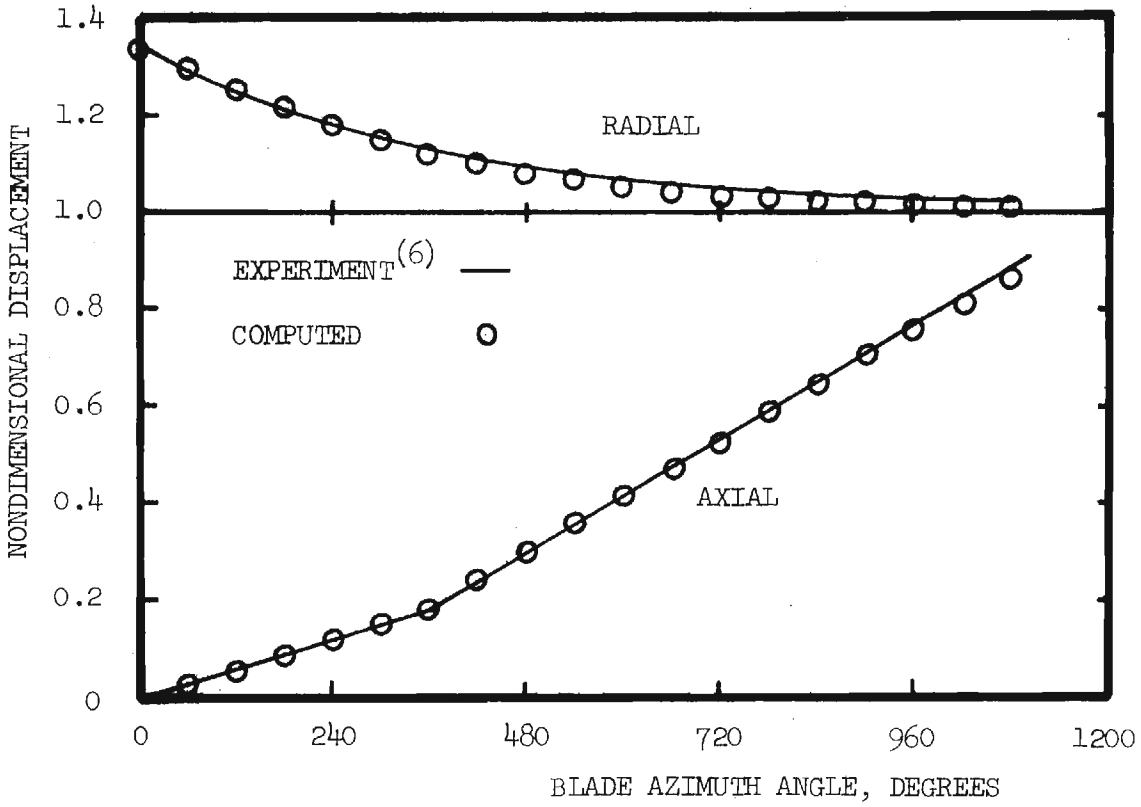

Figure 5. Comparison between measured and computed tip vortex geometry with correction for the vortex core effect.
$C_T = 0.00195$, $b = 1$, $\sigma = 0.040$

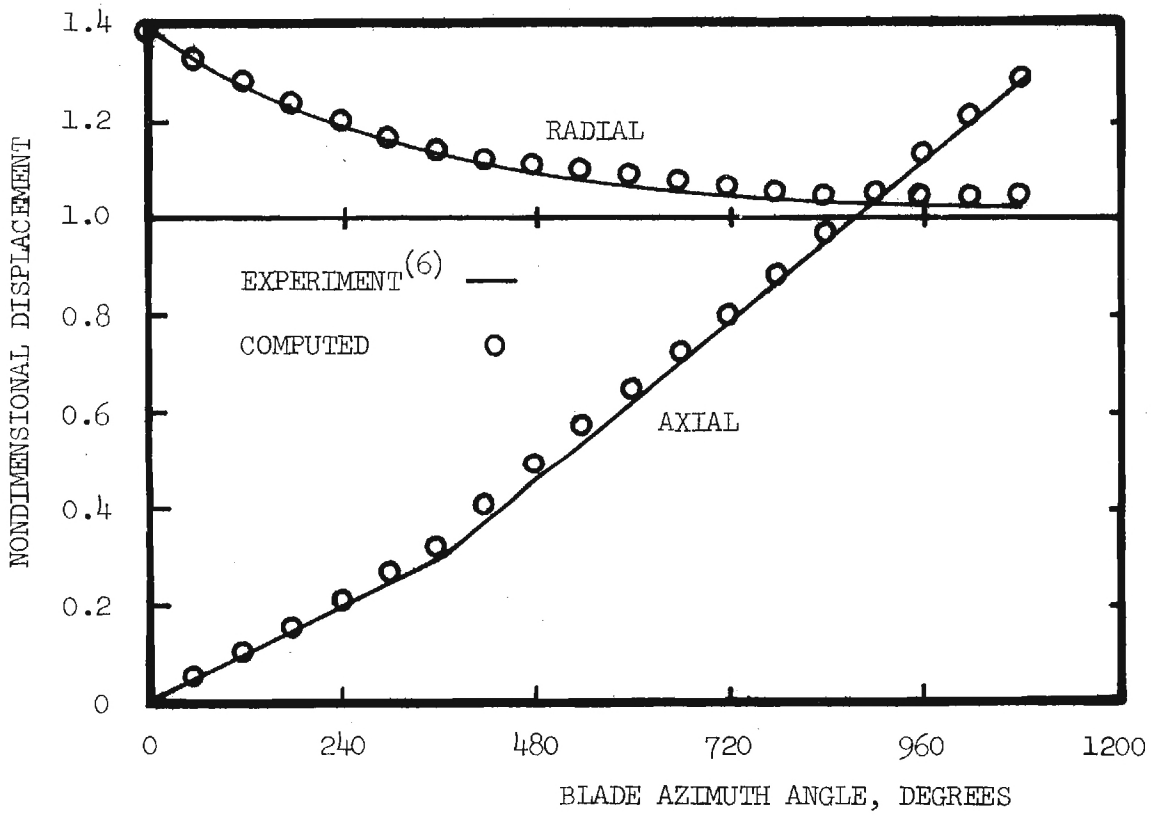

Figure 6. Comparison between measured and computed tip vortex geometry with correction for the vortex core effect.
$C_T = 0.00370$, $b = 1$, $\sigma = 0.040$

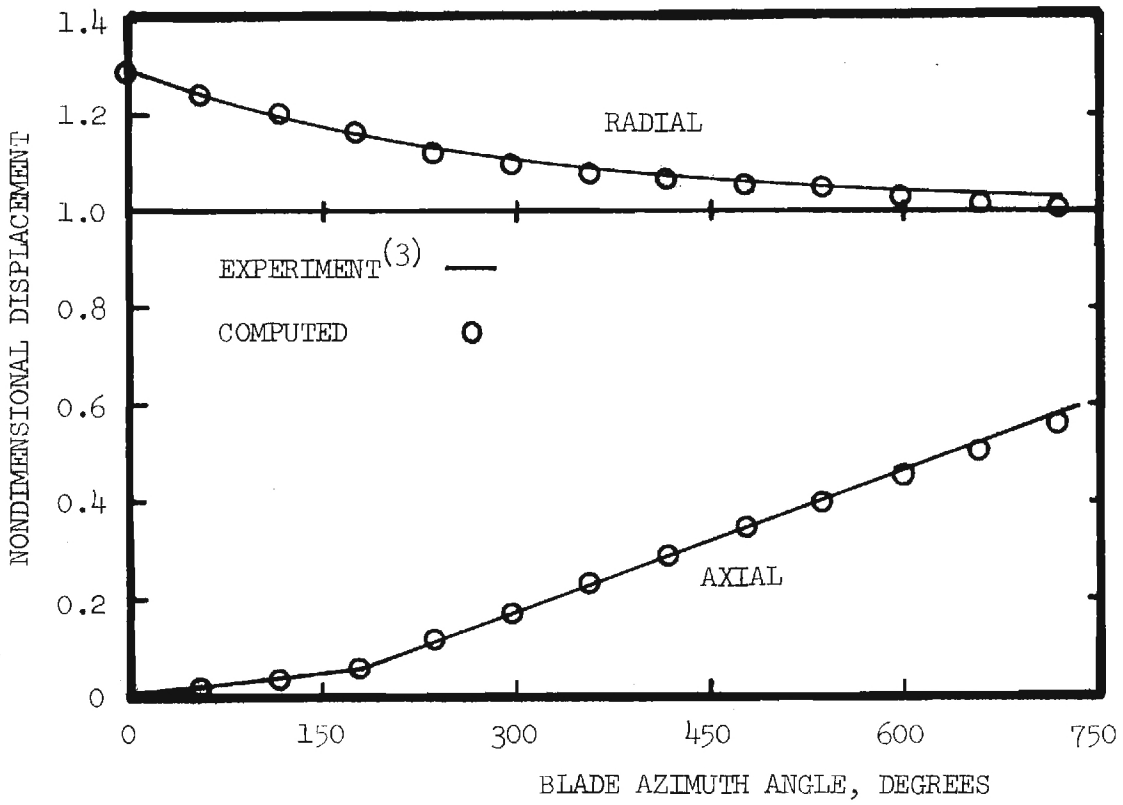

Figure 7. Comparison between measured and computed tip vortex geometry with correction for the vortex core effect.
$C_T = 0.00193$, $b = 2$, $\sigma = 0.070$

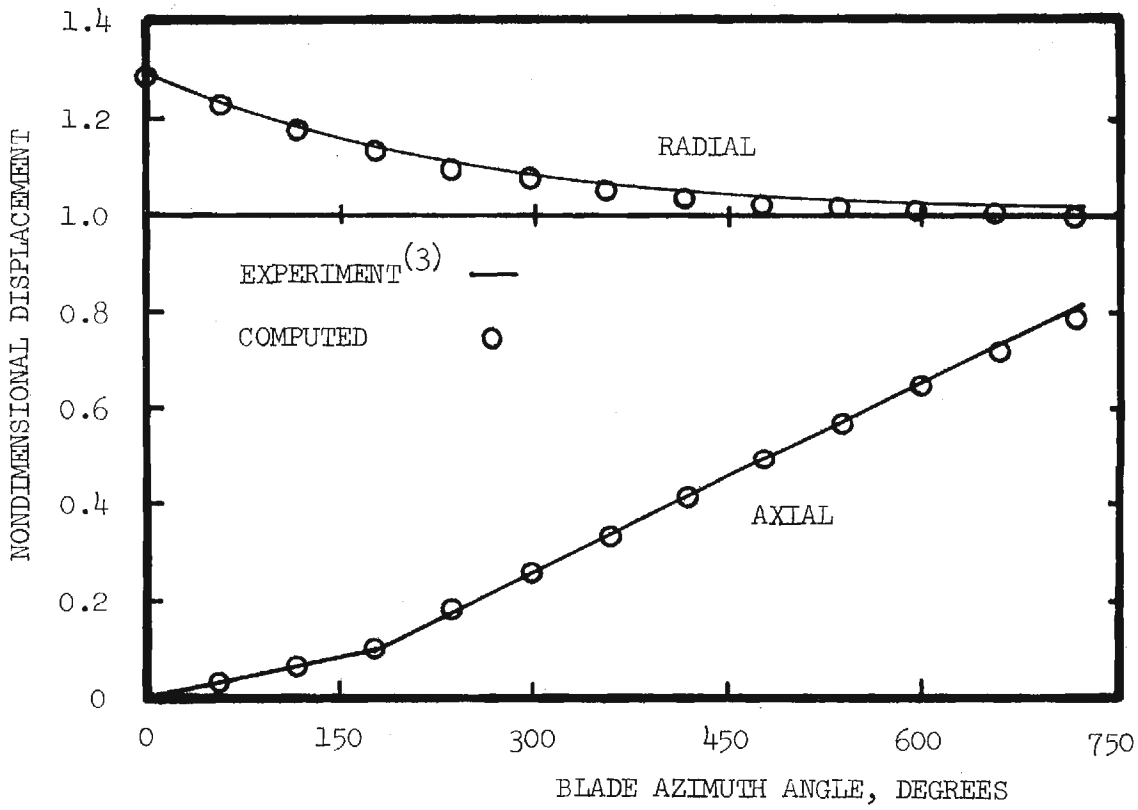

Figure 8. Comparison between measured and computed tip vortex geometry with correction for the vortex core effect.
$C_T = 0.00350$, $b = 2$, $\sigma = 0.070$

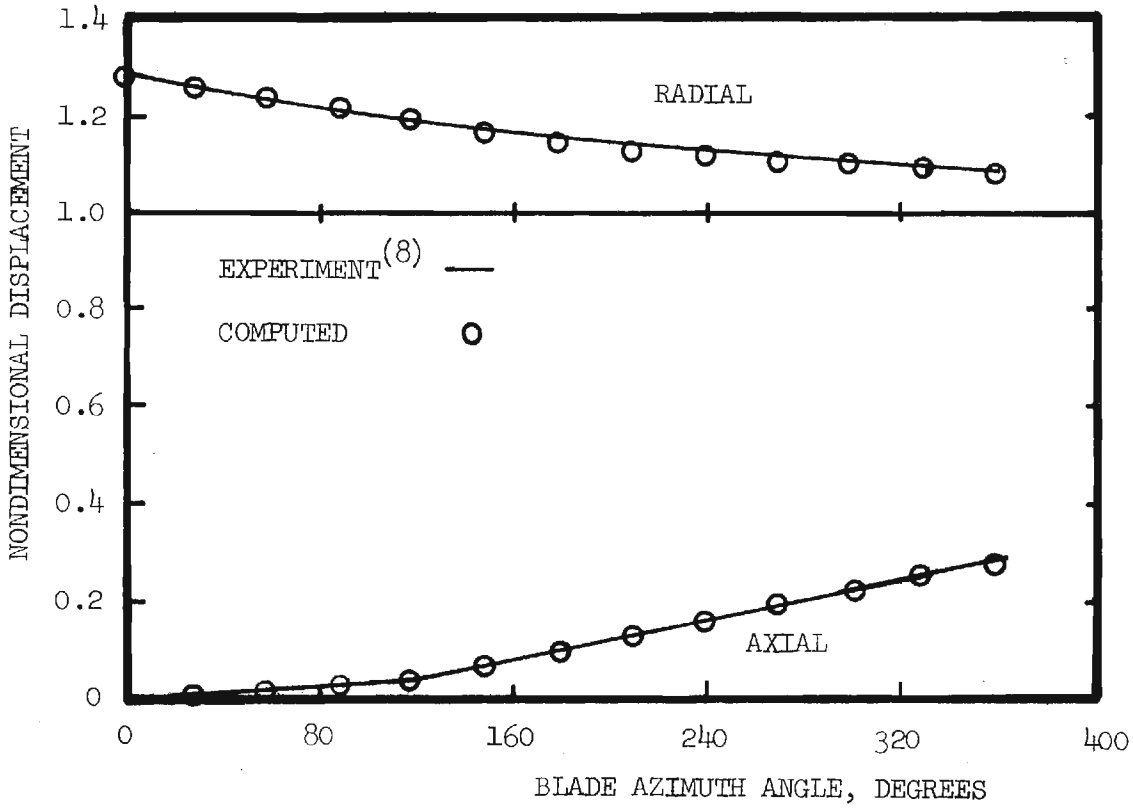

Figure 9. Comparison between measured and computed tip vortex geometry with correction for the vortex core effect.
$C_T = 0.00220$, $b = 3$, $\sigma = 0.105$

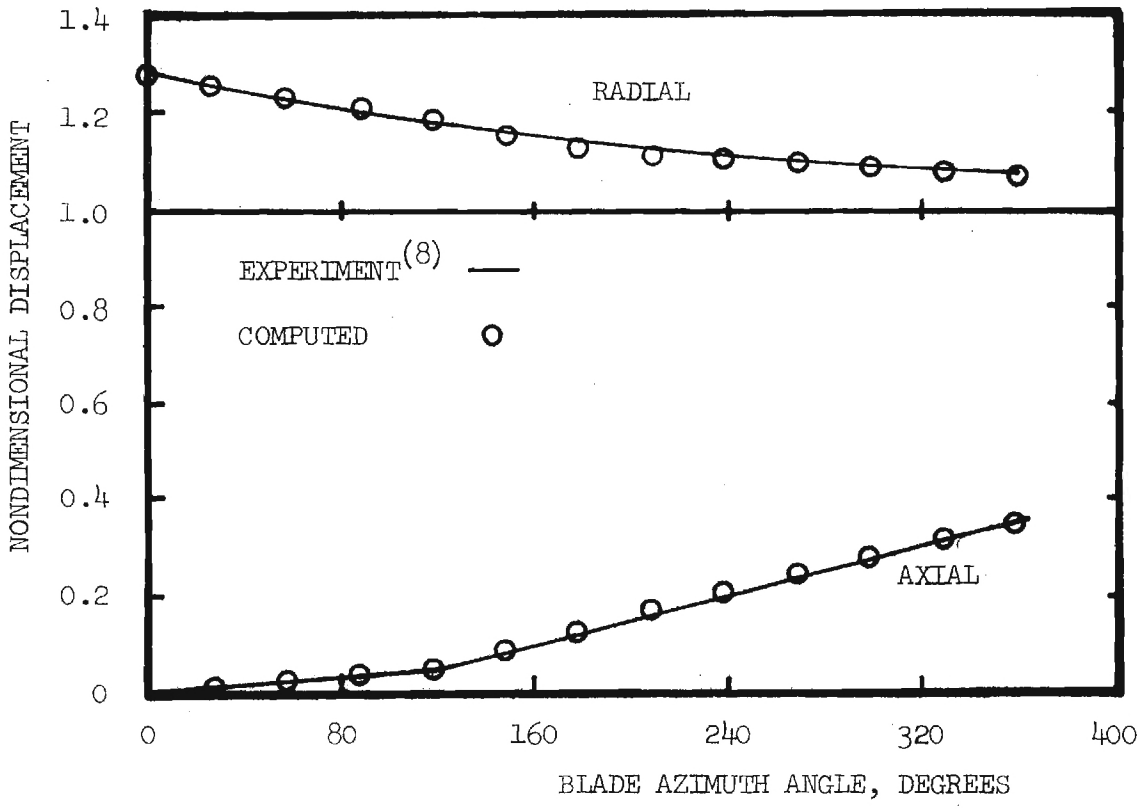

Figure 10. Comparison between measured and computed tip vortex geometry with correction for the vortex core effect.
$C_T = 0.0032$, $b = 3$, $\sigma = 0.105$

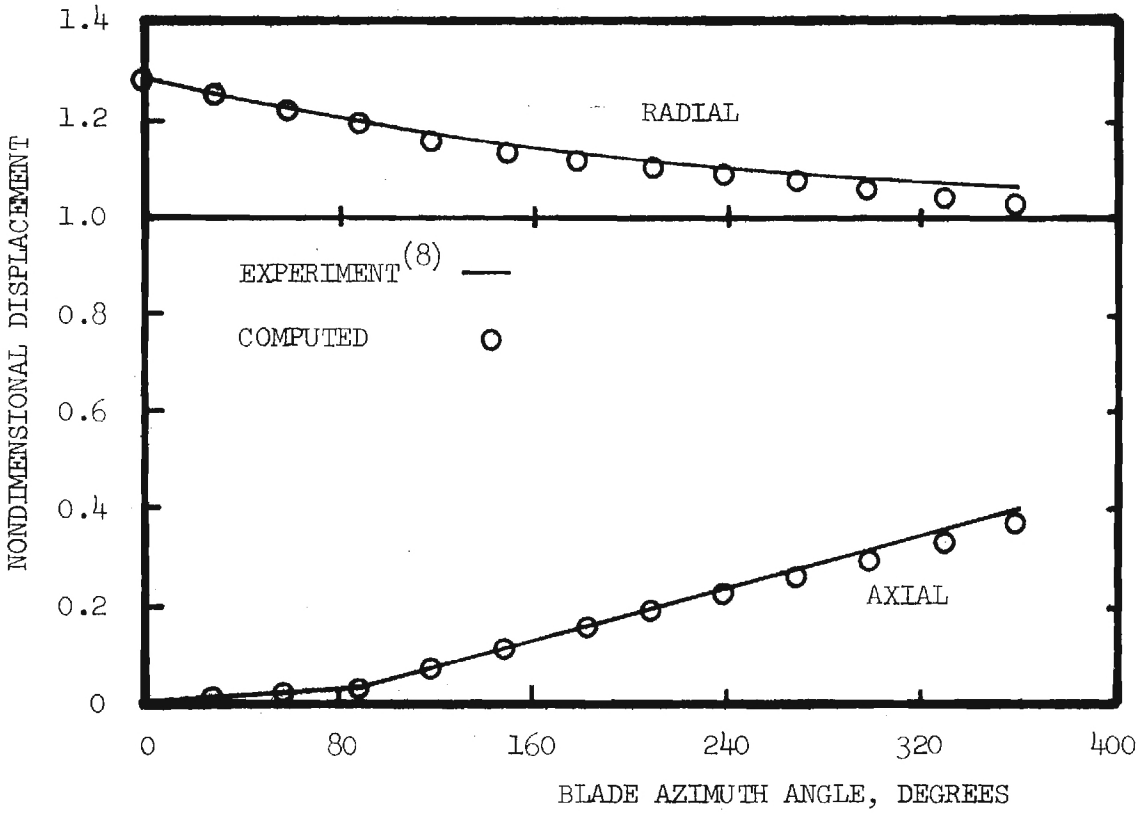

Figure 11. Comparison between measured and computed tip vortex geometry with correction for the vortex core effect.
$C_T = 0.00371$, $b = 4$, $\sigma = 0.140$

for these conditions is not apparent. Although there appears to be a tendency for J to decrease with increasing thrust as shown in Table 1 for the same blade number, it is not clear that any significance can be placed on this or on the observed variation with blade number.

A trial calculation was also attempted for a six-bladed rotor using the measured data of Ref. 3. The method broke down because the iterative procedure for calculating J did not converge. Since this procedure requires the determination of the maximum blade bound vortex strength, this failure is attributed to the use of the lifting line model in close proximity to the tip vortex from the preceding blade. Such a close passage of a blade with the tip vortex of the preceding blade does not occur in the other cases that were considered.

CONCLUDING REMARKS

Studies have been conducted to investigate several modifications which appeared to offer some promise of an improvement of hovering helicopter performance prediction. The effort was directed toward the development of an analysis which would lead to a better agreement between the computed and measured tip vortex geometry. Based on both theoretical and empirical approaches, it was shown that the disagreements that exist in these geometries may be attributed to the lack of a suitable model of the tip vortex core. Semi-empirical correction terms for the core effect were developed. The results were used to compute the tip vortex geometry for a range of thrust coefficients and blade numbers. It was shown that the agreement of the computed geometry with that measured was very much improved for rotors having four or fewer blades. The differences that remain are probably within experimental error. The approach broke down for six-bladed rotors. It appears that this is due to the use of a lifting line rather than a lifting surface model for the blades.

The semi-empirical corrections for the core effect are not considered to be final solutions to the problem. They should be viewed, rather, as worked hypotheses that provide some insight and a stimulus for further investigations directed toward the development of theoretical core models. In this regard, it will be desirable to relate the vortex core structure to the aerodynamic loading on the blade tip and the development of a vortex shedding mechanism. This approach, in turn, may lead to blade tip designs which promote higher axial displacement velocities of the tip vortex and therefore result in a decrease in blade/vortex interaction, particularly for rotors having a greater number of blades. This possibility is suggested by the analysis and would depend upon restructuring the vorticity distribution in the tip vortex core so that its rate of motion down the wake is increased.

Preliminary attempts to incorporate the results into a theoretical vortex wake analysis have disclosed problems in the procedure for determining the tip vortex strength correlation parameter, J. It is suspected, but not shown, that a core model and a shedding mechanism for relating the core structure to the blade tip loading will be required for further improvement of the theoretical analysis.

II. TEST FACILITY

INTRODUCTION

Historically, model helicopter rotors have been tested in "large rooms" in order to reduce the effects of this confinement to a reasonably small level. It has never been clear as to what constitutes a "large room" and it generally has been defined by the space available. The model is then sized to allow clearances of several rotor diameters in all directions. This often results in blades of small dimension which are then difficult to instrument. In addition, various kinds of equipment must sometimes be located near the model and moved around the room as the test program progresses thus modifying the flow environment to some extent. Adequate protection for personnel and equipment can also become a problem. Since large rooms may not be available or must be shared with other experiments for reasons of economy, there is a need for a relatively inexpensive test cell for hovering model rotors that can function in the same manner as a wind tunnel. A test facility that appears to satisfactorily fulfill this function is described below.

This facility has been under development for a number of years. Its design was based on extensive tests of a 1/4 scale model using model airplane propellers. Although the test cell was scaled directly from this model, modifications to the design were required as full-scale experience was gained. It is believed that the modifications were necessary because of the differences in the wake characteristics of the rotor and the propeller.

TEST FACILITY

The longitudinal cross-section of the test cell is shown in Fig. 12. The cell is constructed of wood and has a barricade of steel and wood that extends for a distance of 2 feet on either side of the rotor plane. The interior dimensions are 9 x 9 x 21 feet. The cell is partitioned by a honeycomb which suppresses the turbulence in the return flow. This honeycomb partition has a large circular hole centered on the axis of rotation of the rotor. A bell-mouth duct is installed in this hole and provides for a freer and more uniform passage of the rotor wake. Ventilation ports reduce the incidence and intensity of tornado-like vortices which were observed extending from the thrust side of the rotor to the walls of the cell. Although the flow is not completely smooth, the fluctuations are rather small.

Other components of the facility are as follows:

15 HP, variable-speed drive motor
52-channel mercury slip-ring assembly

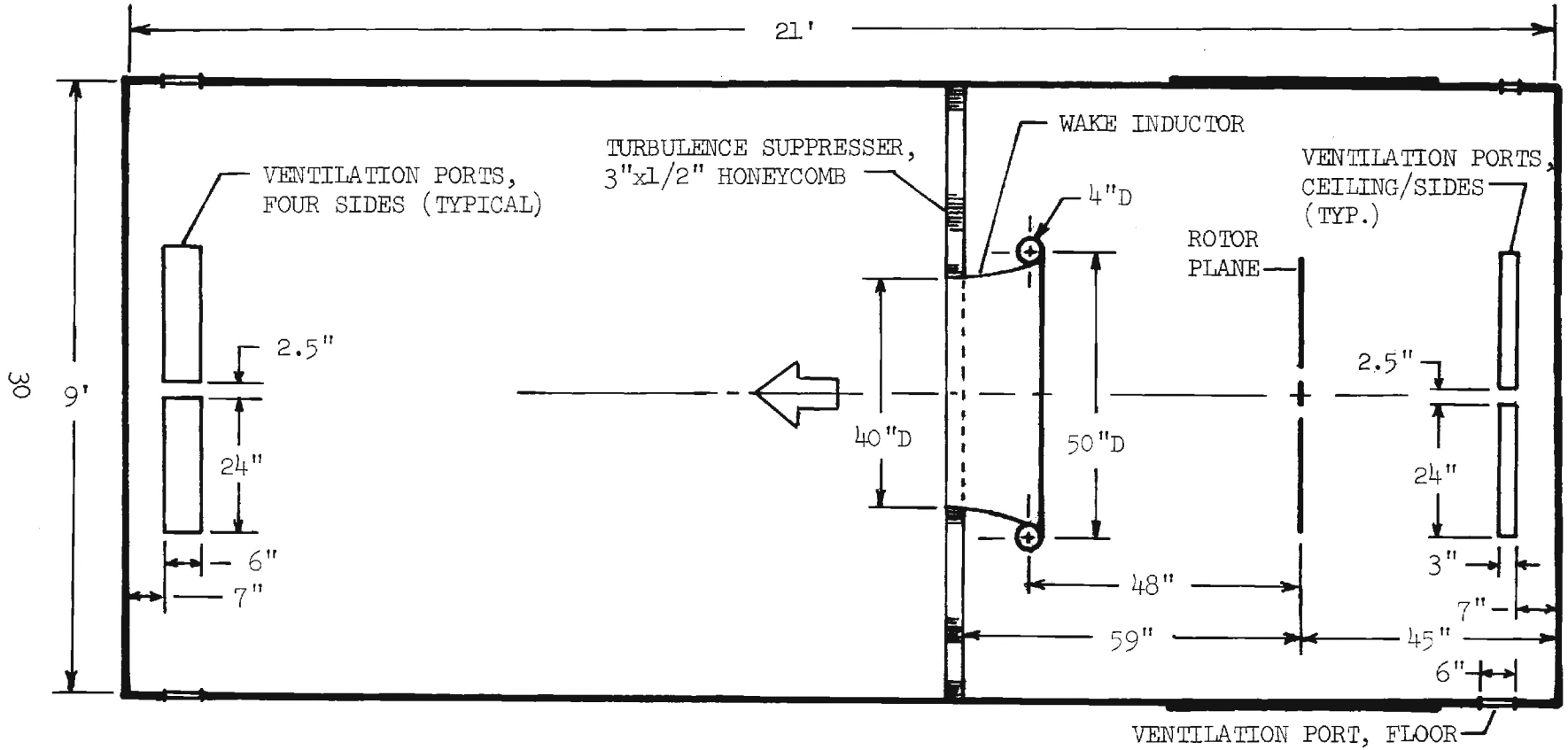

Figure 12. Longitudinal cross-section of hovering test facility for model rotors.

Shaft encoder
Mini-computer with 8K words of memory
Teletype terminal
20-channel scanner
14-channel magnetic tape system
A-D converter
Power supplies, amplifiers, digital voltmeters, electronic counter
Hot-film vector anemometer
Traversing mechanism
Helium bubble generator
Smoke generator
Pressure transducer calibration equipment

In addition, data transfer lines to a central data acquisition system are available which provides a disc storage capability and subsequent data reduction, if desired.

TEST ROTOR AND INSTRUMENTATION

The test rotor has a single, constant-chord, untwisted blade with a square, flat tip and the following geometric characteristics:

Airfoil section	NACA 0012
Blade tip radius	24 inches
Blade chord	5 inches
Collective pitch range	0 - 12 degrees
Solidity	0.0663
Aspect ratio	4.8

These dimensions were established by the size of the test facility and the internal volume required for the installation of the pressure transducers that are described in Part III. Although the model blade is not proportioned according to full-scale practice, the data obtained are satisfactory for guiding the development of theoretical analyses and for comparison with the results of such analyses. The blade is statically balanced with an appropriate counterweight.

The rotor hub is supported on the drive shaft by sixteen flexures whose axes are in the radial direction. Eight of these flexures are positioned at equal azimuth spacings in each of two planes which are perpendicular to the shaft. Such a system in structurally stiff in the radial direction and soft in the axial and tangential directions. The rotor hub is then restrained in these latter two directions by strain-gage beams. One set of beams measures the thrust; the other set, the torque. Positive stops are provided to limit motion of the hub to plus or minus 0.005 inches in the three directions in case of flexure failure. The hub is centered by preloading the beams. A vibration-actuated switch shuts down the drive motor if the rotor dynamic unbalance exceeds a pre-set value. Both aural

and visual alarms are triggered if contact of the hub with the shaft or limit-stops occurs.

The outputs of the strain gage bridge circuits are conducted through the mercury slip rings, amplified, converted from analog to digital signals, and stored in the computer for later tare correction and reduction to standard parametric form.

Initial tests showed that the heat generated by the drive shaft support bearings was conducted into the shaft and to the hub support. This affected both the thrust and torque beam outputs. A thermistor was mounted on the shaft within the hub to measure the temperature and the bearings were oil cooled to reduce the temperature rise. The output drift with temperature could then be determined and its effect on the data removed with the tare corrections.

Rotor speed was determined by electronically counting the pulsed output of a magnetic pickup which sensed the passage of the teeth of a gear which was mounted on the drive shaft. This speed was digitally displayed as revolutions per minute. Since speed is a pre-selected parameter and could be held within plus or minus one revolution per minute, its value was simply entered into the computer's memory.

TEST PROCEDURES

The strain gage beams were calibrated statically and their interactions were determined. The resulting data were curve fitted and the equations were incorporated into the data reduction program. The calibrations were checked periodically.

The contribution of the hub to the total measured torque was determined by running it without the blade and counterweight over a speed range of 120 to 2000 RPM. A pair of dummy counterweights were constructed and installed and the tests were repeated. The torque coefficient required for the hub and one counterweight was calculated to be one-half the sum of that measured at the same RPM in each set of tests. The resulting variation was curve-fitted using a polynomial defined in terms of the RPM so that this source of torque tare could easily be incorporated into the data reduction program. It was assumed that the interference between the hub and counterweight, the two counterweights, and the hub, counterweight, and blade would be negligible (Ref. 9, Chap. VIII).

The blade and counterweight were installed and the rotor was statically and dynamically balanced within acceptable limits. The rotor thrust and blade pitch angle were set to zero by adjusting the pitch angle until there was no flow through the rotor disc. This was accomplished by observing the motion of small, neutrally buoyant, helium-filled, soap bubbles. The rotor was operated over the same speed range as before and the outputs of the thrust and

torque strain gage bridges were recorded. Since the flow through the rotor disc was observed to be zero, the thrust gage output variation with RPM was corrected for the temperature effect and incorporated into the data reduction program as a tare.

The net blade torque coefficients were used in conjunction with blade element theory to compute blade mean profile drag coefficients. The results were compared on the basis of the 3/4 radius Reynolds number with the minimum profile drag coefficients obtained from two-dimensional tests of the NACA 0012 airfoil. The range of the drag coefficients and the shape of the curve versus Reynolds number were good although the curve was shifted to a lower Reynolds number range. This shift may be attributed to the turbulence generated by the blades operating in their own wake which would signify a higher effective Reynolds number than that based only on the blade speed. On the other hand, if there were a net rotation in the wake, the local relative velocities would be less than the local blade speed. If the computed Reynolds numbers and drag coefficients were then based on this lower relative velocity, the former would be reduced and the latter increased. To check these possibilities, the blade pitch angle was set at 0.45° so that the wake would move out of the rotor plane before the next blade passage and the tests were repeated. The new computed mean drag coefficients for the 3/4 radius Reynolds numbers were then about ten percent higher than the corresponding values for the two-dimensional smooth airfoil at the same Reynolds number. Thus, there was a wake effect since the increase was much more than could be attributed to induced drag. Also, these new mean values seemed to be more reasonable in view of the presence of screw heads on the blade surface. (Note: Before computing the drag coefficients, the torque due to the flat blade tip was subtracted from the net blade torque; the quantity subtracted being obtained from the data of Ref. 9, pages 6-4 and 7-21.)

The above tests and calculations were carried out to verify the tare corrections and data reduction procedures. Since the magnitude and variation with Reynolds number of the calculated minimum profile drag coefficient is reasonable, it is believed that the reliability of the net torque data has been established. Although similar tests could not be performed for the thrust data, the procedures were exactly the same and it is assumed that the reliability of the results will be equally good.

The initial tests were run at 120 and 400 RPM and then in steps of 200 RPM up to and including 2,000 RPM. The coverage of this range of rotor speeds involved passing through several resonances of the system. After several of the hub flexures were found to have broken, the maximum speed was restricted to 1350 RPM. Since the flexures could not be visually inspected easily, their condition was checked periodically by rotating the rotor by hand and observing the strain gage bridge outputs. The observed variations were consistently repeatable as long as the flexures were sound. The strain gage

beams were also recalibrated periodically as a check on their reliability and on the condition of the flexures.

Four different test cell configurations were investigated. These were:

1. A closed cell with no internal flow guides;

2. A closed cell with the honeycomb insert at several axial positions;

3. A closed cell with the honeycomb insert and a bell-mouth wake inductor;

4. A ventilated cell with the honeycomb insert and a bell-mouth wake inductor.

For Configurations 1 and 4, tests were performed for a sufficient number of collective pitch angles over the range, 0 to 10°, to adequately define the thrust and torque coefficient variation. A few data points were obtained for Configuration 2 but no quantitative data were taken for Configuration 3. Flow visualization studies of all of the configurations were performed using small, neutrally buoyant, helium-filled, soap bubbles.

Running checks of the data were kept by plotting net thrust and torque versus RPM squared. The variations at the higher Reynolds numbers followed this relationship closely but differed from this relationship at the lower Reynolds numbers in a manner consistent with that of the two-dimensional airfoil section.

Due to the turbulence in the test cell, especially for Configuration 1, the data were obtained by averaging twenty consecutive values which, themselves, were mean values determined by an integrating voltmeter which sampled the strain gage outputs for a period of one second.

RESULTS AND DISCUSSION

The mean blade profile drag coefficient at zero thrust was determined as discussed earlier. Its value is 0.0097 corresponding to a Reynolds number of 564,000 computed for the three-quarter blade radius station. This is about ten per cent higher than that given in Ref. 10 for the smooth two-dimensional airfoil. Since this difference is consistent with the blade surface condition, it was concluded that the tare corrections were correctly accounted for. In addition, this value is required in later calculations of the blade torque.

For the flow visualization studies the nozzle of the helium bubble generator was placed at various positions in the test cell. The bubbles were observed passing directly into the rotor plane at

various positions and being entrained by the wake and the tip vortex. Some of the bubbles were observed to make at least one complete circuit of the wake and the return flow. The starting vortex could be followed as it grew and passed down the wake. After it contacted the walls of the test cell, at a location of about two to three rotor diameters down the wake, its net axial motion ceased and a rotating toroidal mass of turbulent air was formed. The flow in the cell then became established. This flow was more or less stable depending upon the internal configuration of the cell.

For Configuration 1, the closed cell with no internal flow guides, the return flow near the rotor plane was very turbulent with the flow direction changing almost continuously. A varying level in rotor noise was easily heard.

For Configuration 2, the closed cell with a honeycomb insert, the return flow near the rotor plane was much smoother and there was a noticeable reduction in rotor noise. However, abrupt changes in the flow direction were observed. The flow would be relatively steady for a period of ten to fifteen seconds, would then shift to a different direction for a period of several seconds, and then shift back to the initial direction. Although these changes were more or less periodic with time, it was not established that this phenomenon represented a flow field whose position was continually changing in the azimuth direction since all of the observations were performed in the same azimuth plane. A second problem was that the tip vortex did not always pass through the circular cut-out in the honeycomb. The position of the honeycomb was varied between three and five feet downstream from the rotor with no noticeable changes.

An interesting effect was observed when the helium-filled bubbles were introduced into the wake and illuminated with a strobe light which was flashing at the rotor frequency. Some of the bubbles were entrained by the tip vortex, moved rapidly along the vortex core in the direction of blade rotation, and then were expelled from the core. In some cases, the bubbles remained within the core for more than one-half turn of the tip vortex helix. Since the bubbles tended to move down the wake in the plane in which they were introduced, the entrainment of the bubbles by the tip vortex elements which were passing through this plane was continuous. The result was that, with the cell darkened and using strobe illumination, as many as eight half-turns of the helix were observed over an axial distance beneath the rotor of about one rotor diameter. The bubbles within the core appeared to the eye as thin, nearly stationary, segmented lines of reflected strobe light and were observed for many blade revolutions. Thus, the tip vortex seemed to be stable for Configuration 2 although the return flow was not.

Configuration 3 was obtained by installing a bell-mouth inlet in the circular cut-out of the honeycomb insert. The passage of the wake through the bell mouth appeared to be freer but there were

essentially no changes in the return flow characteristics, the thrust and torque measurements, or in the noise level. Flow visualization studies were conducted in greater detail in the inflow region near the rotor. It was discovered that tornado-like vortices occasionally formed between the thrust side of the rotor and the walls of the test cell. These vortices would move around in a random manner for several seconds before dissipating, only to form again later at a different location.

In previous conversations with Dr. F. H. Schmitz of the Ames Directorate, USAAMDRL, he had suggested that it might become necessary to ventilate the test cell. This was done as shown in Fig. 12. Flow visualization studies were again conducted. It was verified that the return flow was improved, that only minor fluctuations remained, and that the perceived rotor noise was further reduced in level. No other modifications to the facility were made since the flow in the cell now appeared to be satisfactory.

Complete thrust and torque measurements over a blade pitch angle range of 0 to 10° were made with the cell in Configurations 1 and 4. A few data points were obtained for Configuration 2 but none for Configuration 3 since no changes were apparent. The net blade thrust and torque coefficient variations with blade pitch angle are given in Figs. 13 and 14. Fig. 13 shows that there is no significant difference in the measured thrust coefficients between Configurations 1 and 2 and Configuration 4. This difference can be explained by considering the thrust and torque equations that are obtained by applying blade element theory.

The thrust equation that is based on blade element theory has a term that is proportional to the inflow angle. Therefore, assumed time variations of the inflow about a mean value will not appreciably affect the computed thrust when the computed thrust itself is a time averaged quantity. Then, the significance of Fig. 13 is that the mean value of the rotor inflow for a given thrust level is essentially the same for all test cell configurations. However, the similarly derived torque equation includes terms that are proportional to the square of the inflow angle. In this case, assumed time variations of the inflow about a mean value will affect the computed torque even when the computed torque is also a time averaged quantity. Thus, it appears that the rotor performance in the test cell was primarily affected by the presence of the tornado-like vortices that formed in the flow field between the thrust side of the rotor and the walls of the cell since the elimination (or reduction in intensity) of these vortices resulted in improved performance. Fig. 14 also shows that the data tend to converge as the blade pitch angle approaches zero.

Although the flow in Configuration 4 seemed to be satisfactory, it was not clear that the measured performance was essentially the same as that which would be measured for the isolated rotor. It

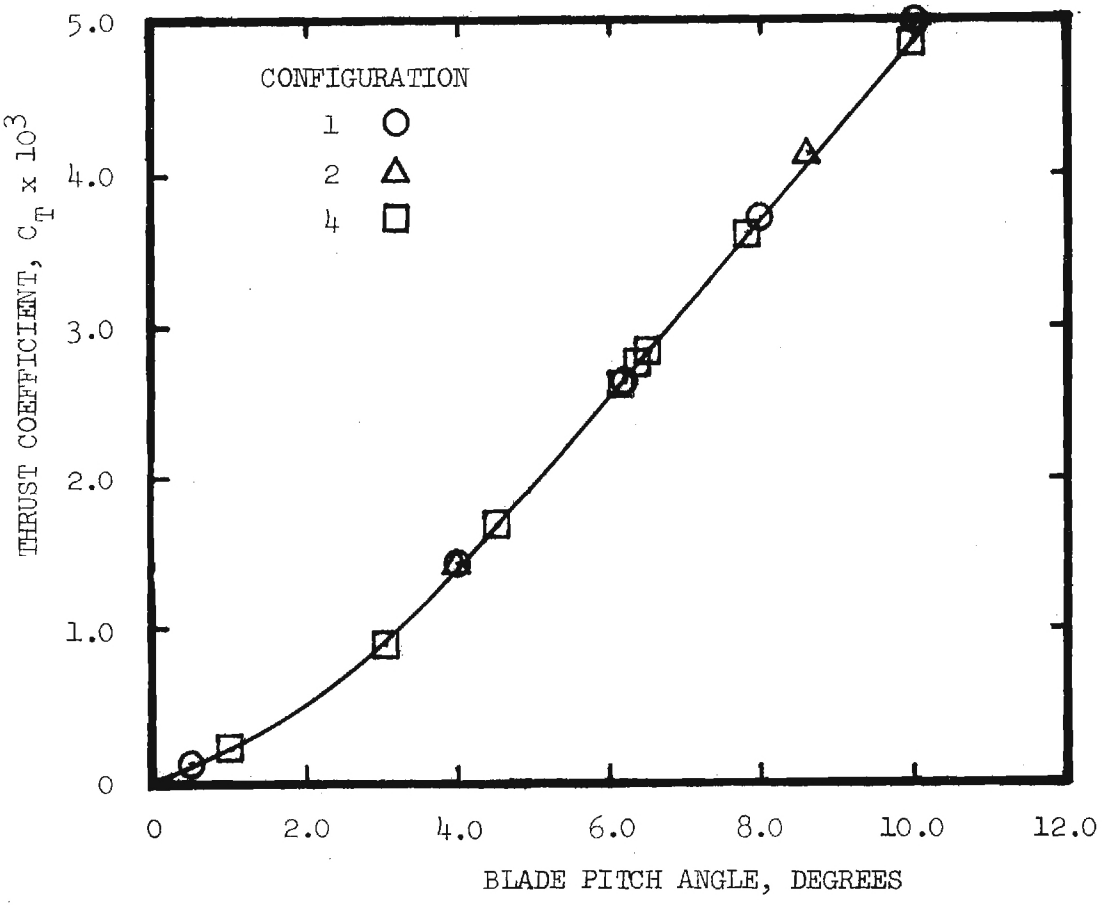

Figure 13. Thrust coefficient variation of a single-bladed model rotor versus blade pitch angle for various internal configurations of the test facility. Reynolds No. (3/4 Radius) $\sim 0.56 \times 10^6$, $\sigma = 0.0663$.

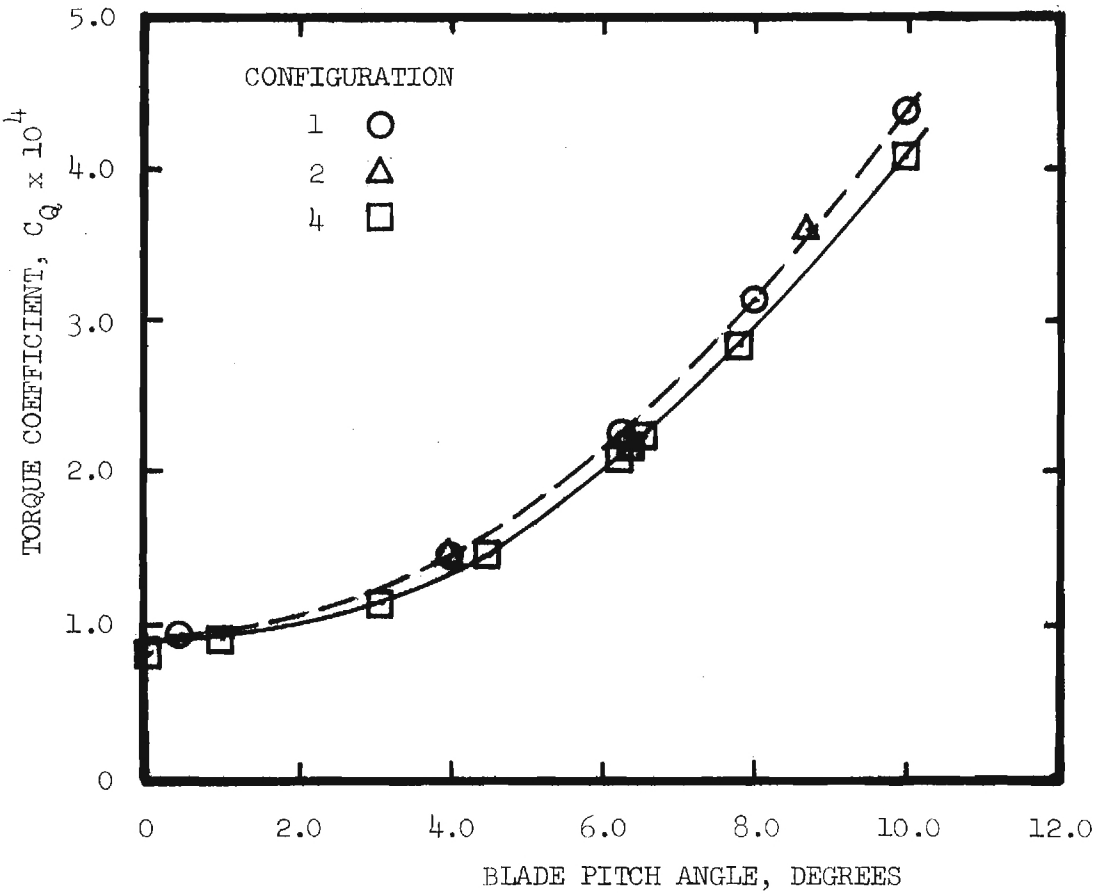

Figure 14. Torque coefficient variation of a single-bladed model rotor versus blade pitch angle for various internal configurations of the test facility. Reynolds No. (3/4 Radius) $\sim 0.56 \times 10^6$ $\sigma = 0.0663$.

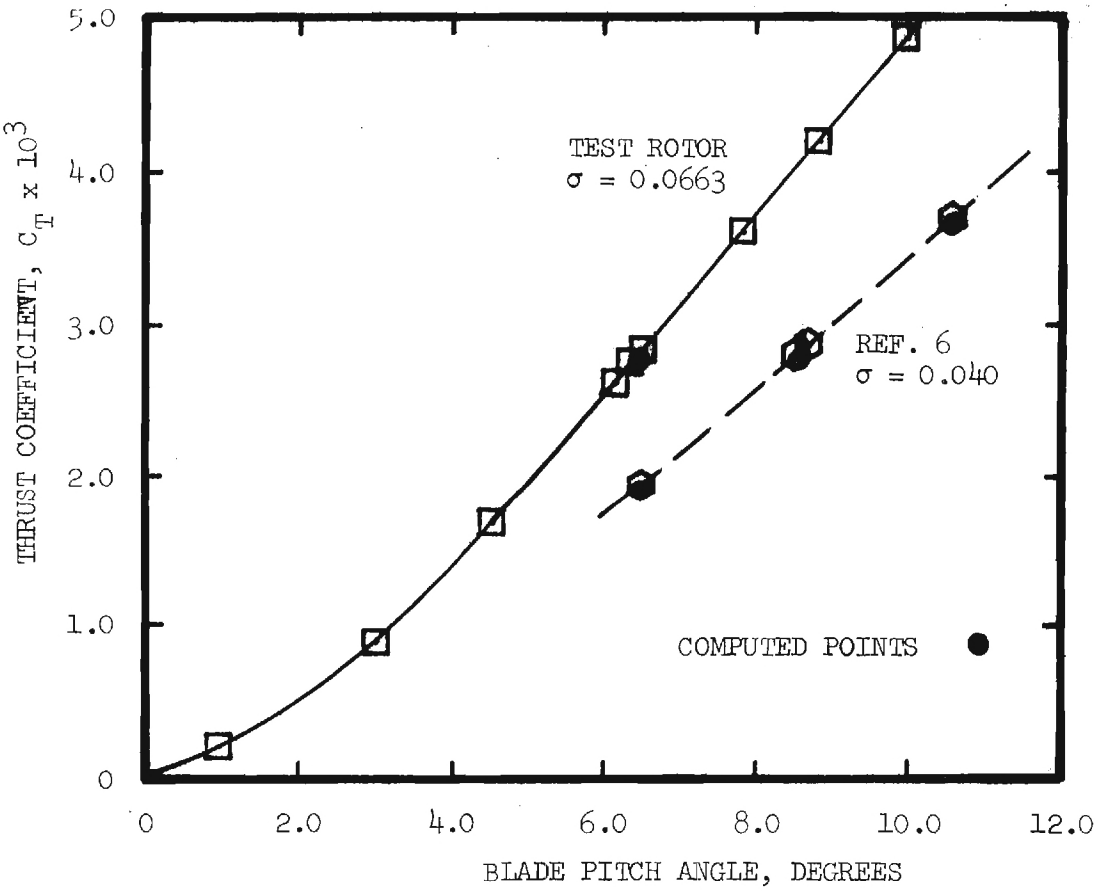

Figure 15. Measured thrust coefficient variation with blade pitch angle for two single-bladed rotors of different solidity and a comparison with computed values. Reynolds No. (3/4 Radius) $\sim 0.56 \times 10^6$.

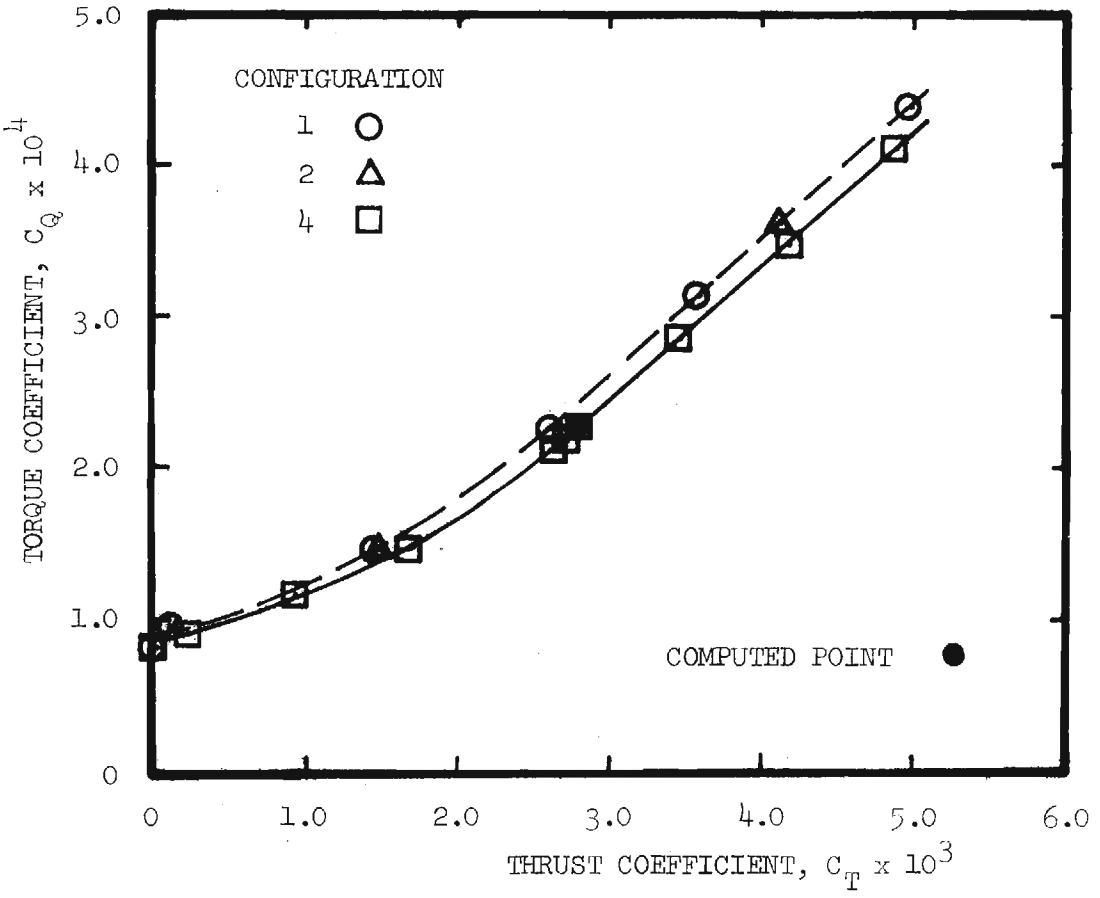

Figure 16. Torque coefficient variation of a single-bladed model rotor versus thrust coefficient for various internal configurations of the test facility and a comparison with a computed value for an isolated rotor. Reynolds No. (3/4 Radius) $\sim 0.56 \times 10^6$, $\sigma = 0.0663$.

would, of course, be desirable to test the model rotor in a very large room and then to compare the measured performance with that obtained from the test facility. Since this was not possible, another means had to be found to determine the degree of confinement to which the model would be subjected in the test cell.

The approach, then, was to compare the measured performance with that obtained from a prescribed vortex wake analysis. The required input data for beginning this analysis are available in Ref. 6 for a single-bladed rotor tested in a large room at approximately the same blade Reynolds number as that of the model. For a Reynolds number of approximately 560,000 at the three-quarter blade radius, the lift curve slope is obtained from Ref. 10 as 5.41 per radian. To substantiate the approach, the thrust performance of the rotor of Ref. 6 was computed and is compared with the corresponding measured values in Fig. 15. Although the computed thrust is shown to be consistently low, the agreement is good. A similar computation was performed for the model and equally as good an agreement is shown in the figure. In both cases, the use of a slightly higher value of the lift curve slope in the calculations would have yielded exact agreement. It is concluded that as far as the integrated thrust is concerned, the model is essentially operating as an isolated rotor.

In order to compute the torque, not only is a value for the lift curve slope required in the blade element analysis but also a relationship between the section profile drag coefficient and the corresponding lift coefficient. Such a relationship is given in Ref. 11 and this was used in the computations except that the mean value determined previously for the blade minimum profile drag coefficient was used instead of that for the two-dimensional airfoil. The result of one calculation is shown in Fig. 16 and the agreement is very good.

In spite of the good agreement between the computed and measured values of the thrust and torque coefficients, it is not clear that the computed aerodynamic loading would agree equally as well with that which exists on the model blade hovering in the test facility. However, there is an indication that the loading near the blade tip may be essentially the same as that for the isolated rotor. For example, Fig. 22 of Section III compares the computed two-dimensional chordwise pressure distribution with the measured distribution at $r/R = 0.94$. The effective angle of attack used in the calculation is that obtained from the prescribed wake analysis for the lifting line at the same radial station. The agreement between the peak pressures and the distributions over the first 15 per cent of the chord is good. Therefore, it would appear that the interference of the test cell on the flow in the tip region is small. The observed differences in the pressure distributions are attributed to tip relief, boundary layer effects, and the local shedding of the tip vortex.

Since the rotor is not instrumented to measure the pressure distribution on the entire blade, another approach is required to establish the effect of the test cell on the aerodynamic loading. Present plans are to measure the axial induced velocity distribution near the rotor disk and to compare it with the distribution computed by the prescribed wake analysis for the isolated rotor. Although this approach will not yield direct blade angle of attack distributions, it will provide a good qualitative indication of the effect of the test cell on the inflow and then, by inference, on the angle of attack distribution.

CONCLUDING REMARKS

It has been shown that the computed thrust and torque coefficients for the isolated rotor agree closely with the measured coefficients for the model rotor hovering in the test facility. It has not been established that the aerodynamic loadings for the two cases will agree equally as well. However, there is an indication that the effect of the test cell confinement on the inflow near the blade tip is small so that the pressure distributions measured in this region will be satisfactory for guiding and substantiating theories which may be developed for predicting tip-loss effects and for modeling tip vortex shedding mechanisms.

III. BLADE TIP PRESSURE DISTRIBUTIONS

INTRODUCTION

The operating characteristics of rotary wing vehicles are strongly influenced by the vortex wake of the rotating blades. The dominant feature of this wake is the helical vortex which has its origin at the tip of the rotor. Rotor theory has progressed to the point where a detailed knowledge of the structure of the tip vortex is needed, implying a need for better understanding of the mechanism of tip vortex formation. Furthermore, the tip section of a rotor blade plays a much more important role in providing lift than does the wing tip of a fixed-wing vehicle because the dynamic pressure is much higher near the rotor tip than on the inboard section of the rotor. Thus the traditional approach in performance calculations of using some "tip loss factor" needs to be made more precise. There is therefore a strong requirement for more detailed knowledge of the aerodynamic environment very near the tip of a helicopter rotor blade.

Flow visualization tests (Ref. 12) have given qualitative information on the local flow direction near the rotor tip. Other experiments on blade-vortex interaction (Refs. 13,14) and tip vortex abatement (Ref. 15) have given some insight into the tip problem. These studies mainly have dealt with unsteady pressure distributions over the entire blade due to blade-vortex interactions. There are no detailed data at the rotor tip.

The tip vortex generated by a fixed wing has received considerable attention (Refs. 16,17,18,19). Measurement of surface pressure distribution over square tips has shown the presence of a primary vortex as well as a secondary vortex near the tip on the top surface of the lifting wing. The applicability of fixed wing results to rotating wings has been investigated using flow visualization (Refs. 16,17). The results indicate that the location of the tip vortex is affected by centrifugal force but that, at least from these qualitative results, it may be possible to carry over wing results to hovering rotors.

It is the aim of this study to provide detailed surface pressure distribution data very near the tip of a single-bladed helicopter rotor in hover. Data were obtained at collective pitch angles of zero, 6.2, and 11.4 degrees at blade RPM's of 1000 and 1350 corresponding to tip Reynolds numbers (based on chord) of 0.544×10^6 and 0.736×10^6.

BLADE TIP ASSEMBLY

The test rotor has a constant chord, untwisted blade with an NACA 0012 airfoil section. The blade chord is 5 inches and the tip

radius is 24 inches. The outermost 1.75 inches of the blade is made of magnesium and is removable. This removable tip was fabricated in two pieces of equal width in the spanwise direction which were cemented with epoxy along the chordwise interface and held together by through-bolts. Before the two pieces were cemented together, matching holes of diameters ranging from 0.203" to 0.0625" were drilled into each piece and groups of these holes were joined together by slots milled in the mating surfaces so as to form six cavities (see Figs. 17 and 18). The largest hole in each group was drilled through the inboard side of the assembly and tapped to receive a transducer mounting plug. Surface pressure orifices 0.025" in diameter were then drilled from the airfoil surface into the six cavities. These orifices were located in chordwise planes at the 94.0, 96.6, 98.0, 98.7, 99.1, and 99.5 per cent blade radius stations. In each plane, an orifice was located at the airfoil leading edge and 20 holes were located on both the upper and lower surfaces. The square, flat outboard tip was drilled with 25 orifices, nine of which were distributed along the chord line and the remaining 16 arranged symmetrically with respect to the chord line.

The transducer plugs extended approximately 0.70" into the cavities and had a milled flat on which was cemented a paddle-type subminiature pressure transducer. The four wires from each transducer were led through a small hole in the plug, along slots cut into the interface between the removable tip and the blade, and thence along a tube inside the blade to a terminal block on the rotor hub. Care was taken in machining the flats and cutting the threads on the plugs so that when the plugs were seated the flats containing the transducers were perpendicular to the airfoil chordline. This was done so as to minimize the effects of inertial forces on the transducer output.

After checking that no orifices were plugged and that there were no leaks between cavities, the two tip pieces were epoxied together and the plugs and lead-wires were cemented with RTV. Finally, the assembly was checked and made as leak-tight as possible. The removable tip then consisted of six irregularily-shaped cavities, each of which had a free volume of approximately 0.06 cubic inches and contained a pressure transducer which was exposed to airfoil surface pressure through the several orifices drilled into the cavity. During a data run, pressures were measured at 6 surface locations (i.e. in 6 cavities) at one time, the remaining pressure orifices being covered with tape. A typical cavity is shown in Figure 18.

INSTRUMENTATION

Surface pressures were measured using Sensotec Type SA-8J-7F1 paddle gages. These gages have an active 4-arm bridge bonded to a stainless steel diaphragm 1/8" in diameter. The nominal output is 1 mv/psi per volt of excitation and the stated sensitivity of these gages to inertial loads tangential to the diaphragm surface is about 0.09 mv/1000 "g". These transducers are temperature-compensated but

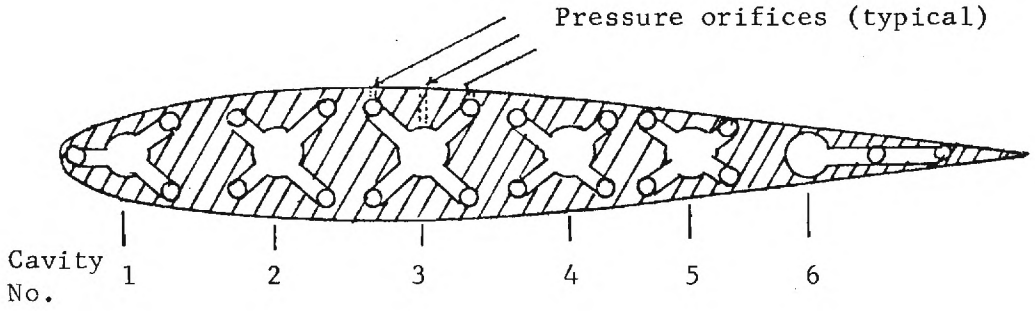

Figure 17. Cross-section of removable tip at mating surface

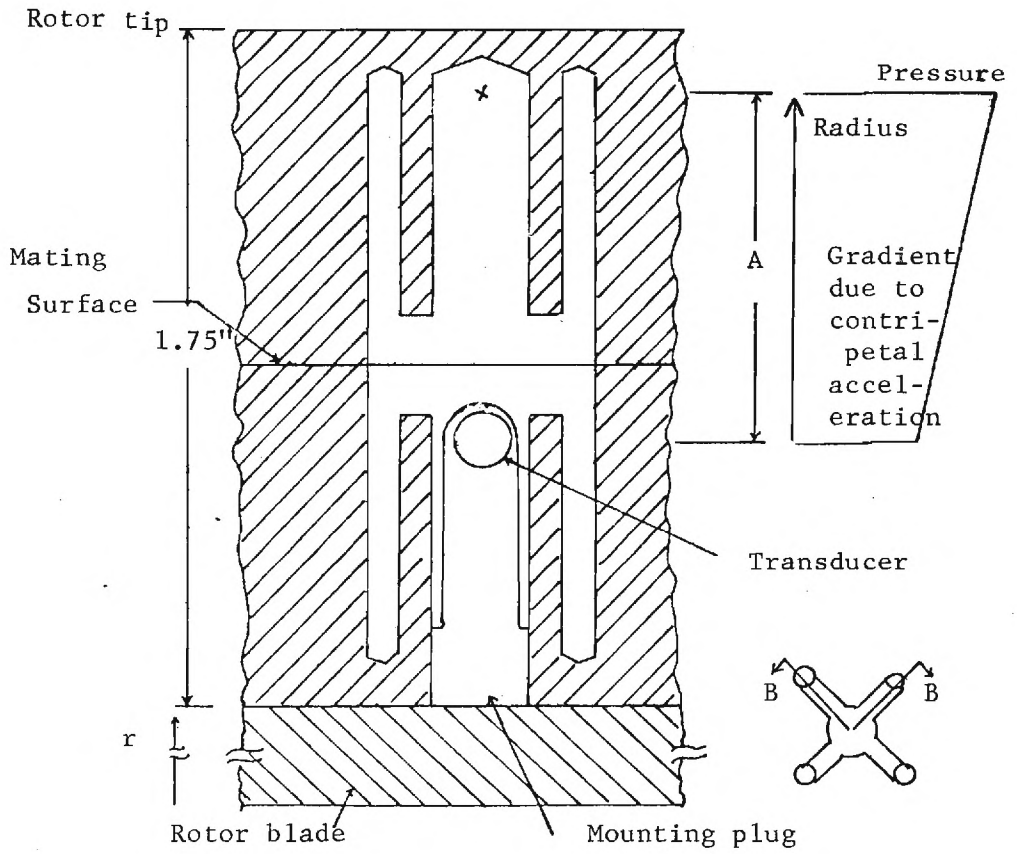

Figure 18. Section of a typical cavity

the air temperature in the rotor test chamber did not vary over 2-3 degrees F even after trial runs of 20 minutes duration. To avoid inaccuracies due to changes in slip ring resistance, zero adjustment of the transducer bridge must be performed on the hub rather than after the slip rings. This complication was eliminated by accepting the small zero offset of the gages since the resulting voltage output in the tests was not large enough to saturate the amplifiers. A Kulite Type CQL-080-5 transducer was mounted flush with the rotor surface at the 90.6% radial station and 7.5% chord station on the thrust side of the blade. This gage has a outside diameter of .08" and an output of .485 mv/psi per volt of excitation. This transducer has a good frequency response since it was flush-mounted. It was used in preliminary tests to confirm that the surface pressure on the rotating blade is essentially constant with time. Thus, the poor frequency response characteristics of the cavities does not affect the surface pressure measurements.

The output of the transducers was conducted from the rotor hub through mercury slip rings to Neff Type 122 DC amplifiers set at a gain of 200. The signals then were routed through a scanner to a HP2401C integrating digital volt meter (DVM). Data acquisition was accomplished with a HP 2114 mini-computer with teletype output.

The transducers were statically calibrated in place by applying a known pressure to each cavity and to the reference transducer. This known pressure was measured with a Barocel electronic manometer which was calibrated using a dead-weight tester.

PROCEDURE

a) Static Calibration - An air-tight lucite box was installed over the end of the rotor blade and sealed at its inboard with an O-ring around the blade contour. This box was pressurized with nitrogen through a low-pressure regulator. The box pressure (which was varied between zero and 2 psi) was read on a Barocel electronic manometer while the corresponding output of the pressure transducers was read with the integrating DVM. With 3 volts excitation, the output of the gage in cavity 6 was 1.337 mv/psi while the gages in the other five cavities had outputs in the range of 2.244 to 2.917 mv/psi (before amplification). The output of all gages was linear with applied pressure and repeatable with 1.5%. There was only a 1.5% difference in slope when compared with transducer static calibrations done several months previously. The static calibration was repeated weekly during the data-taking period of 7 weeks.

b) Acceleration Corrections - When diaphragm-type pressure transducers are installed in an accelerating system, the resulting inertial load on the diaphragm results in a diaphragm deflection and an output signal which is indistinguishable from that due to an applied pressure. The magnitude of this output signal depends on the orienta-

tion of the inertial force with respect to the diaphragm. In the present application, the centripetal acceleration of the rotor blade results in an inertial load of 1200 g's at the gage radial position at 1350 RPM. The gages were carefully installed to ensure that this load was tangential to the diaphragm. Even so, the "g" correction is appreciable compared to the pressure signal. Thus the "g" correction had to be evaluated accurately. The method employed here was to measure this correction with the gages in place by sealing off all of the pressure orifices with tape and running the blade up to operating RPM. The resulting output of the gages is then due to the inertia loading on the diaphragm and on the column of air trapped in the cavity. (See Fig. 18). The net effect of the inertia loading on the air column is to reduce the pressure at the transducer and this reduction may be calculated for a given RPM. The determination of the correction for the inertial loading on the diaphragm proved to be more of a problem. Since the free volume of the cavities is small, a small leak into or out of this closed volume will result in a change in the pressure of the air trapped in the cavity. Thus, instead of a constant output due to "g" forces, the gage will display a slowly changing output due to the leak. It should be noted that very small leaks which will cause a problem here would not be as significant during the surface pressure measurements when a "large" pressure orifice is open to the surface and overpowers the leak. Several different types of sealing tape were tried in the "g" correction tests but all gave unacceptable leaks. The final solution was to cover the tip with strips of Scotch brand Number 471 plastic tape and then to paint the tape with Spraylat Corporation's "Sign-Strip". The strippable paint gave a thin leak resistant plastic-like finish and was easily removed. While there still may have been minute leaks around the plug threads, the outputs of the transducer during "g" calibration were essentially constant with RPM. The "g" correction varied from gage to gage in the range 0.05-0.30 mv at 1200 "g" and was repeatable within ± 0.02 mv.

The pressure gradient due to the "g" effects on the air column within the cavity must also be accounted for in the measurement of the surface pressure if the pressure orifice is at a different radial location than the transducer diaphragm. For example, there is a correction due to the dimension "A" in Fig. 18. The uncorrected chordwise pressure distribution at a typical radial station is shown in Fig. 19 together with the pressure distribution obtained by applying the three "g" corrections noted above. Also shown in Fig. 19 is the magnitude of the "g" correction due to inertia force, air column (orifices closed) and air column (orifice open) for a typical gage at 94.27% radius.

c) Data Acquisition - Data were taken in the same manner for both the "g" correction tests and the surface pressure measurements, the only difference being that in the "g" tests the tip was covered with tape and then coated with strippable paint whereas in the pressure measurements the tip was covered with tape and then one orifice into each cavity was opened by piercing the hole with a needle. Preliminary

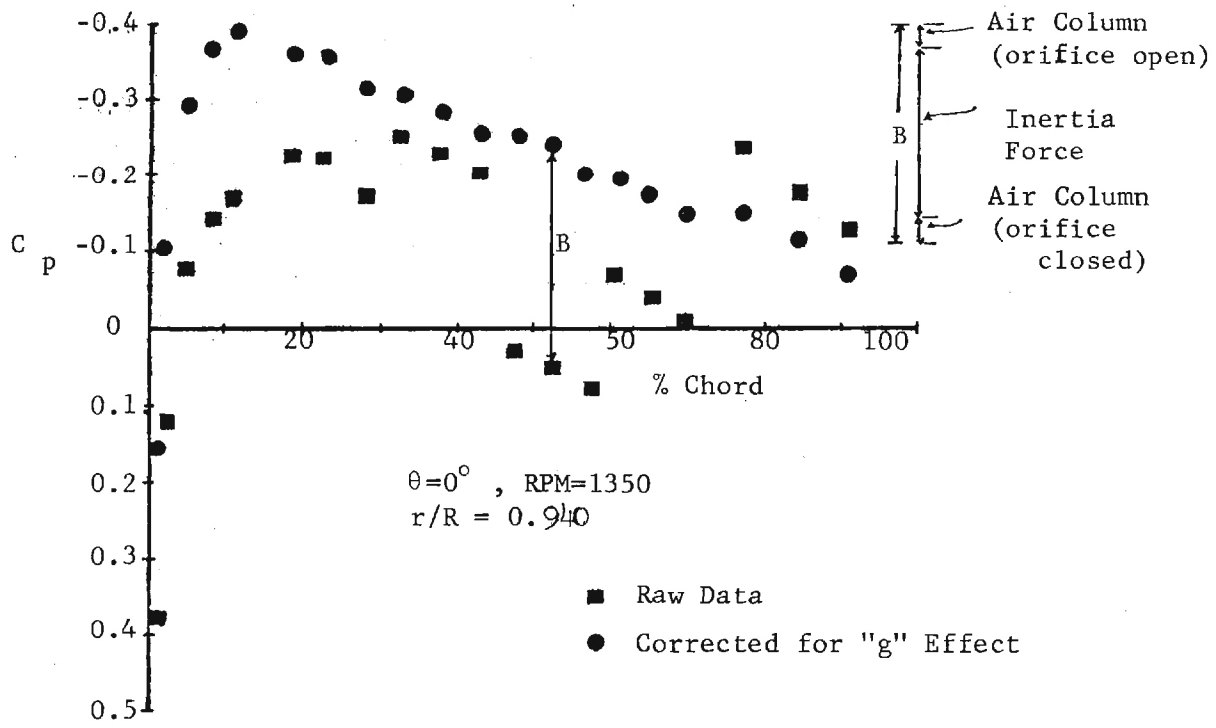

Figure 19. Effect of centripetal acceleration correction.

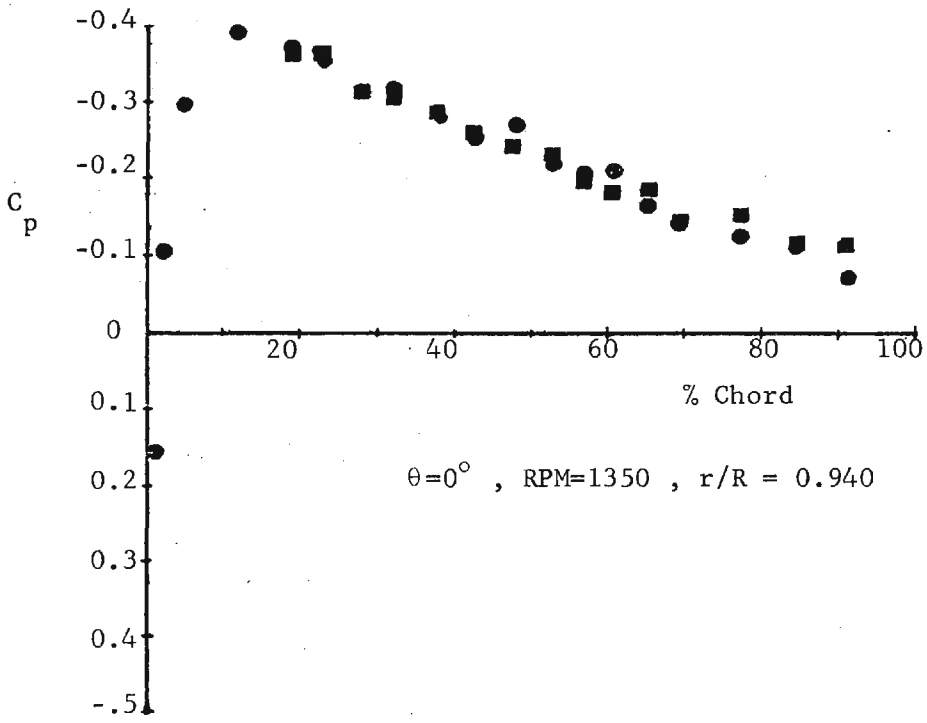

Figure 20. Typical repeatability

tests with different tape orientations and thicknesses indicated that the measured pressures were not affected by the presence of the tape. The six transducer voltages were read with the DVM set to integrate and average over 0.1 second and were printed out on the teletype. Before starting a test, a sample of 6 readings was taken every 20 seconds to establish the zero drift. An acceptable zero drift of the gage output was a change of less than 10 microvolts per one minute. If the zero drift was acceptable, the rotor was brought up to the desired RPM in less than 30 seconds. The outputs of the six transducers were measured and recorded. At least 3 readings were taken for each transducer within a time interval of one minute. The rotor was then stopped in less than 20 seconds and the zero readings were repeated with sufficient samples to ensure that an acceptable zero drift had been maintained. The value of pressure was calculated by subtracting the initial zero reading from the first pressure measurement and the final zero reading from the last pressure measurement taken in the one minute time interval and then forming the average of the two differences. After correcting for acceleration effects the data were expressed in C_p form by using the ambient air density and the local blade velocity. The rotor tip was retaped after every run. Repeatability checks were routinely made in the course of filling out the pressure distribution data.

At zero thrust and 1350 RPM, a typical transducer (e.g. cavity 2) gave an unamplified output of 0.50 mv (of which 0.18 mv was due to "g" effects) with respect to the zero offset and with three volts excitation. The repeatability of the pressure coefficient data from the experiments is shown in Fig. 20. It is estimated that the data is accurate to within ± 5 percent.

RESULTS AND DISCUSSION

Surface pressure measurements on the rotor near the tip ($r/R \geq 0.94$) were made at blade pitch angles of 0°, 6.2°, and 11.4° at Reynolds numbers (based upon rotor tip speed and chord) of 0.544×10^6 (1000 RPM) and 0.736×10^6 (1350 RPM). The data were reduced to pressure coefficient form by using the dynamic pressure corresponding to the blade velocity at the appropriate radial station. All of the results are tabulated in Tables 2 through 8. The columns headed Row 1, Row 2, and Row 3 refer to the pressures measured on the flat tip of the rotor. Row 1 is located 0.037 chord length above the chord line of the symmetric rotor airfoil section; Row 2, along the chord line; and Row 3, 0.0375 chord length below the chord line.

The pressure distributions at zero degrees and 1350 RPM are plotted in Fig. 21. It is seen that at the innermost station ($r/R = 0.94$) the agreement with conventional two-dimensional airtoil theory is good over the first fifty percent of the chord. As one goes toward the tip, the suction peaks on the airfoil are seen to decrease because of a three-dimensional relief effect. At the outermost station

TABLE 2. PRESSURE COEFFICIENT DISTRIBUTION ON UPPER SURFACE AND FLAT TIP
PITCH ANGLE=0 DEGREES , RPM=1350

% CHORD	RADIAL POSITIONS r/R						FLAT TIP			% CHORD
	0.940	0.966	0.980	0.987	0.991	0.995	ROW1	ROW2	ROW3	
.0	.897	.891	.875	.861	.867	.809				.0
1.0	.157	.079	.097	.072	.080	.051				1.0
2.0	-.104	-.098	-.153	-.179	-.151	-.193		-.461		2.0
5.0	-.295	-.299	-.288	-.292	-.291	-.292				5.0
7.5	-.368	-.351	-.340		-.305	-.305		-.158		7.5
10.5				-.327	-.298	-.292				10.5
11.5	-.390	-.365	-.347				-.329		-.338	11.5
18.5	-.362	-.344	-.293				-.194		-.150	18.5
21.5				-.278	-.244	-.219				21.5
22.5	-.358	-.336	-.306	-.261	-.236	-.220		-.075		22.5
27.5	-.313	-.296	-.240	-.217	-.205	-.186	-.110		-.085	27.5
32.5	-.309	-.261	-.230	-.207	-.197	-.175	-.072		-.068	32.5
37.5	-.287	-.250	-.218	-.214	-.194	-.170		-.044		37.5
42.5	-.256	-.235	-.210	-.192	-.193	-.165	-.062		-.066	42.5
47.5	-.256	-.236	-.219	-.193	-.176	-.178	-.076		-.082	47.5
52.5	-.233	-.220	-.178	-.176	-.173	-.163		-.089		52.5
56.5	-.200	-.193	-.153	-.161	-.154	-.178	-.080		-.088	56.5
60.5	-.196	-.172	-.152	-.149	-.157	-.167	-.108		-.112	60.5
65.0	-.172	-.155	-.145	-.144	-.160	-.170		-.095		65.0
69.0	-.143	-.121	-.135	-.131	-.150	-.190				69.0
77.0	-.150	-.151	-.162	-.145	-.187	-.197		-.140		77.0
84.4	-.113	-.130	-.129	-.145	-.160	-.182		-.115		84.4
91.0	-.069	-.116	-.100	-.130	-.163	-.197		-.089		91.0
93.0								.113		93.0

TABLE 3, PRESSURE COEFFICIENT DISTRIBUTION ON UPPER SURFACE AND FLAT TIP
PITCH ANGLE=6.2 DEGREES , RPM=1350

% CHORD	RADIAL POSITIONS r/R						FLAT TIP			% CHORD
	0.940	0.966	0.980	0.987	0.991	0.995	ROW1	ROW2	ROW3	
.0	.807	.812	.836	.835	.868	.849				.0
1.0	-.665	-.650	-.596	-.475	-.438	-.460				1.0
2.0	-.812	-.734	-.722	-.652	-.593	-.561		-.621		2.0
5.0	-.806	-.715	-.639	-.607	-.559	-.517				5.0
7.5	-.752	-.680	-.613	-.560	-.513	-.460		-.178		7.5
10.5				-.504	-.459	-.408				10.5
11.5	-.685	-.615	-.539				-.188		-.442	11.5
18.5	-.535	-.468	-.415				-.126		-.280	18.5
21.5				-.359	-.330	-.284				21.5
22.5	-.472	-.444	-.398	-.364	-.315	-.276		-.088		22.5
27.5	-.412	-.380	-.320	-.300	-.266	-.247	-.134		-.227	27.5
32.5	-.385	-.310	-.269	-.264	-.247	-.249	-.114		-.198	32.5
37.5	-.334	-.267	-.262	-.254	-.241	-.258		-.064		37.5
42.5	-.293	-.271	-.250	-.245	-.245	-.266	-.145		-.133	42.5
47.5	-.276	-.262	-.246	-.248	-.251	-.375	-.145		-.134	47.5
52.5	-.249	-.231	-.239	-.239	-.263	-.502		-.167		52.5
56.5	-.233	-.220	-.218	-.225	-.287	-.532	-.180		-.120	56.5
60.5	-.226	-.216	-.203	-.218	-.331	-.548	-.201		-.131	60.5
65.0	-.211	-.202	-.200	-.205	-.382	-.516		-.190		65.0
69.0	-.193	-.178	-.203	-.222	-.444	-.479				69.0
77.0	-.183	-.162	-.182	-.280	-.461	-.448		-.185		77.0
84.4	-.121	-.133	-.176	-.379	-.455	-.416		-.174		84.4
91.0	-.109	-.119	-.149	-.395	-.421	-.365		-.157		91.0
93.0								.123		93.0

TABLE 4. PRESSURE COEFFICIENT DISTRIBUTION ON LOWER SURFACE
PITCH ANGLE=6.2 DEGREES , RPM=1350

% CHORD	RADIAL POSITIONS r/R						% CHORD
	0.940	0.966	0.980	0.987	0.991	0.995	
.0	.887	.862	.847	.861	.867	.845	.0
1.0	.630	.626	.549	.543	.502	.426	1.0
2.0	.398	.380	.314	.287	.216	.165	2.0
5.0	.132	.029	-.014	-.010	-.038	-.079	5.0
7.5	-.064	-.088	-.097	-.098	-.104	-.133	7.5
10.5				-.153	-.144	-.175	10.5
11.5	-.158	-.154	-.162				11.5
18.5	-.170	-.173	-.172				18.5
21.5				-.162	-.149	-.152	21.5
22.5	-.173	-.181	-.181	-.150	-.159	-.149	22.5
27.5	-.180	-.180	-.179	-.162	-.151	-.138	27.5
32.5	-.200	-.191	-.178	-.162	-.154	-.147	32.5
37.5	-.202	-.185	-.171	-.154	-.145	-.139	37.5
42.5	-.191	-.169	-.162	-.140	-.140	-.127	42.5
47.5	-.191	-.179	-.162	-.154	-.147	-.138	47.5
52.5		-.169	-.158	-.132	-.134	-.136	52.5
56.5	-.174	-.159	-.153	-.134	-.139	-.126	56.5
60.5	-.168	-.164	-.121	-.139	-.135	-.129	60.5
65.0	-.167	-.154	-.145	-.123	-.134	-.125	65.0
69.0	-.159	-.145	-.139	-.124	-.126	-.117	69.0
77.0	-.145	-.148	-.145	-.132	-.122	-.117	77.0
84.4	-.134	-.133	-.129	-.109	-.104	-.104	84.4
91.0	-.088	-.106	-.122	-.109	-.109	-.084	91.0

TABLE 5. PRESSURE COEFFICIENT DISTRIBUTION ON UPPER AND LOWER SURFACES
PITCH ANGLE= 11.4 DEGREES , RPM=1350

% CHORD	RADIAL POSITIONS r/R					% CHORD
	0.995		0.991	0.987	0.966	
	UPPER SURFACE	LOWER SURFACE	UPPER SURFACE	UPPER SURFACE	UPPER SURFACE	
.0		.641		.510		.0
1.0						1.0
2.0	-.917	.356	-1.017	-1.126	-1.411	2.0
5.0						5.0
7.5	-.634		-.720	-.796		7.5
10.5	-.528		-.613			10.5
11.5						11.5
18.5						18.5
21.5	-.422		-.438	-.460		21.5
22.5	-.425	-.130	-.420	-.430	-.531	22.5
27.5	-.391	-.116	-.376	-.378		27.5
32.5	-.452	.000	-.346	-.349		32.5
37.5	-.623	-.116	-.361	-.351	-.344	37.5
42.5	-.758	-.112	-.389	-.332		42.5
47.5						47.5
52.5						52.5
56.5						56.5
60.5	-.604		-.731	-.444		60.5
65.0	-.579	-.134	-.711	-.509	-.250	65.0
69.0	-.605		-.698	-.589		69.0
77.0	-.588		-.631	-.683		77.0
84.4	-.588		-.628	-.777	-.163	84.4
91.0	-.501	-.067	-.551	-.719		91.0

TABLE 6. PRESSURE COEFFICIENT DISTRIBUTION ON UPPER SURFACE AND FLAT TIP
PITCH ANGLE=0 DEGREES , RPM=1000

% CHORD	RADIAL POSITIONS r/R						FLAT TIP			% CHORD
	0.940	0.966	0.980	0.987	0.991	0.995	ROW1	ROW2	ROW3	
.0	.936	.921	.916	.898	.901	.845				.0
1.0	.212	.133	.135	.098	.114	.090				1.0
2.0	-.063	-.051	-.103	-.128	-.112	-.152		-.457		2.0
5.0	-.253	-.250	-.241	-.242	-.233	-.243				5.0
7.5	-.296	-.304	-.292	-.267	-.263	-.267		-.166		7.5
10.5				-.275	-.261	-.252				10.5
11.5	-.336	-.311	-.299				-.293		-.308	11.5
18.5	-.320	-.301	-.262				-.177		-.140	18.5
21.5				-.241	-.224	-.198				21.5
22.5	-.330	-.300	-.265	-.242	-.223	-.204		-.069		22.5
27.5	-.289	-.259	-.221	-.198	-.172	-.183	-.092		-.058	27.5
32.5	-.276	-.235	-.207	-.181	-.174	-.159	-.054		-.051	32.5
37.5	-.256	-.223	-.194	-.184	-.172	-.164		-.023		37.5
42.5	-.234	-.207	-.186	-.172	-.166	-.135	-.048		-.050	42.5
47.5	-.224	-.226	-.186	-.157	-.176	-.180	-.073		-.057	47.5
52.5	-.199	-.179	-.170	-.120	-.159	-.136		-.084		52.5
56.5	-.184	-.172	-.170	-.130	-.138	-.155	-.062		-.092	56.5
60.5	-.169	-.159	-.155	-.113	-.127	-.134	-.080		-.081	60.5
65.0	-.154	-.138	-.111	-.119	-.134	-.138		-.070		65.0
69.0	-.117	-.113	-.100	-.104	-.117	-.147				69.0
77.0	-.107	-.092	-.105	-.085	-.105	-.173		.094		77.0
84.4	-.077	-.047	-.081	-.091	-.105	-.140		-.060		84.4
91.0	-.051	-.060	-.069	-.105	-.113	-.145		-.115		91.0
93.0								.057		93.0

TABLE 7. PRESSURE COEFFICIENT DISTRIBUTION ON UPPER SURFACE AND FLAT TIP
PITCH ANGLE=6.2 DEGREES , RPM=1000

% CHORD	RADIAL POSITIONS r/R						FLAT TIP			% CHORD
	0.940	0.966	0.980	0.987	0.991	0.995	ROW1	ROW2	ROW3	
.0	.842	.836	.872	.877	.908	.890				.0
1.0	-.621	-.609	-.561	-.424	-.405	-.421				1.0
2.0	-.760	-.673	-.683	-.605	-.559	-.517		-.633		2.0
5.0	-.763	-.681	-.597	-.552	-.520	-.457				5.0
7.5	-.703	-.639	-.560	-.519	-.468	-.416		-.141		7.5
10.5				-.453	-.410	-.368				10.5
11.5	-.638	-.577	-.495				-.147		-.403	11.5
18.5	-.514	-.446	-.388				-.122		-.278	18.5
21.5				-.344	-.305	-.263				21.5
22.5	-.475	-.412	-.362	-.336	-.292	-.262		-.077		22.5
27.5	-.422	-.370	-.325	-.282	-.239	-.232	-.121		-.199	27.5
32.5	-.382	-.315	-.262	-.248	-.236	-.243	-.119		-.185	32.5
37.5	-.335	-.264	-.246	-.241	-.232	-.239		-.063		37.5
42.5	-.272	-.248	-.230	-.226	-.243	-.264	-.141		-.119	42.5
47.5	-.120	-.239	-.219	-.213	-.274	-.344	-.183		-.117	47.5
52.5	-.228	-.231	-.203	-.231	-.254	-.463		-.145		52.5
56.5	-.223	-.205	-.191	-.196	-.281	-.493	-.160		-.087	56.5
60.5	-.187	-.177	-.177	-.184	-.301	-.511	-.175		-.100	60.5
65.0	-.171	-.168	-.169	-.185	-.352	-.465		-.158		65.0
69.0	-.154	-.152	-.158	-.194	-.417	-.436				69.0
77.0	-.149	-.147	-.144	-.254	-.436	-.453		-.174		77.0
84.4	-.100	-.114	-.157	-.354	-.430	-.423		-.174		84.4
91.0	-.069	-.080	-.120	-.356	-.448	-.367		-.165		91.0
93.0								.051		93.0

TABLE 8, PRESSURE COEFFICIENT DISTRIBUTION ON LOWER SURFACE
PITCH ANGLE=6.2 DEGREES , RPM=1000

% CHORD	RADIAL POSITIONS r/R						% CHORD
	0.940	0.966	0.980	0.987	0.991	0.995	
.0	.920	.904	.887	.906	.909	.885	.0
1.0	.677	.670	.592	.594	.547	.468	1.0
2.0	.443	.429	.372	.327	.264	.210	2.0
5.0	.173	.072	.032	.029	.007	-.030	5.0
7.5	-.017	-.036	-.048	-.043	-.098	-.089	7.5
10.5				-.105	-.052	-.127	10.5
11.5	-.105	-.112	-.110				11.5
18.5	-.151	-.152	-.145				18.5
21.5				-.139	-.116	-.126	21.5
22.5	-.155	-.152	-.145	-.113	-.134	-.132	22.5
27.5	-.159	-.158	-.149	-.120	-.129	-.124	27.5
32.5	-.181	-.169	-.162	-.145	-.134	-.134	32.5
37.5	-.173	-.161	-.147	-.134	-.134	-.119	37.5
42.5	-.167	-.149	-.135	-.140	-.129	-.109	42.5
47.5	-.180	-.160	-.182	-.118	-.177	-.117	47.5
52.5		-.137	-.139	-.135	-.096	-.088	52.5
56.5	-.149	-.148	-.119	-.151	-.162	-.080	56.5
60.5	-.135	-.119	-.108	-.100	-.093	-.098	60.5
65.0	-.121	-.119	-.101	-.089	-.105	-.079	65.0
69.0	-.115	-.100	-.094	-.094	-.082	-.072	69.0
77.0	-.116	-.107	-.122	-.108	-.109	-.130	77.0
84.4	-.072	-.087	-.090	-.075	-.105	-.075	84.4
91.0	-.072	-.081	-.072	-.121	-.087	-.069	91.0

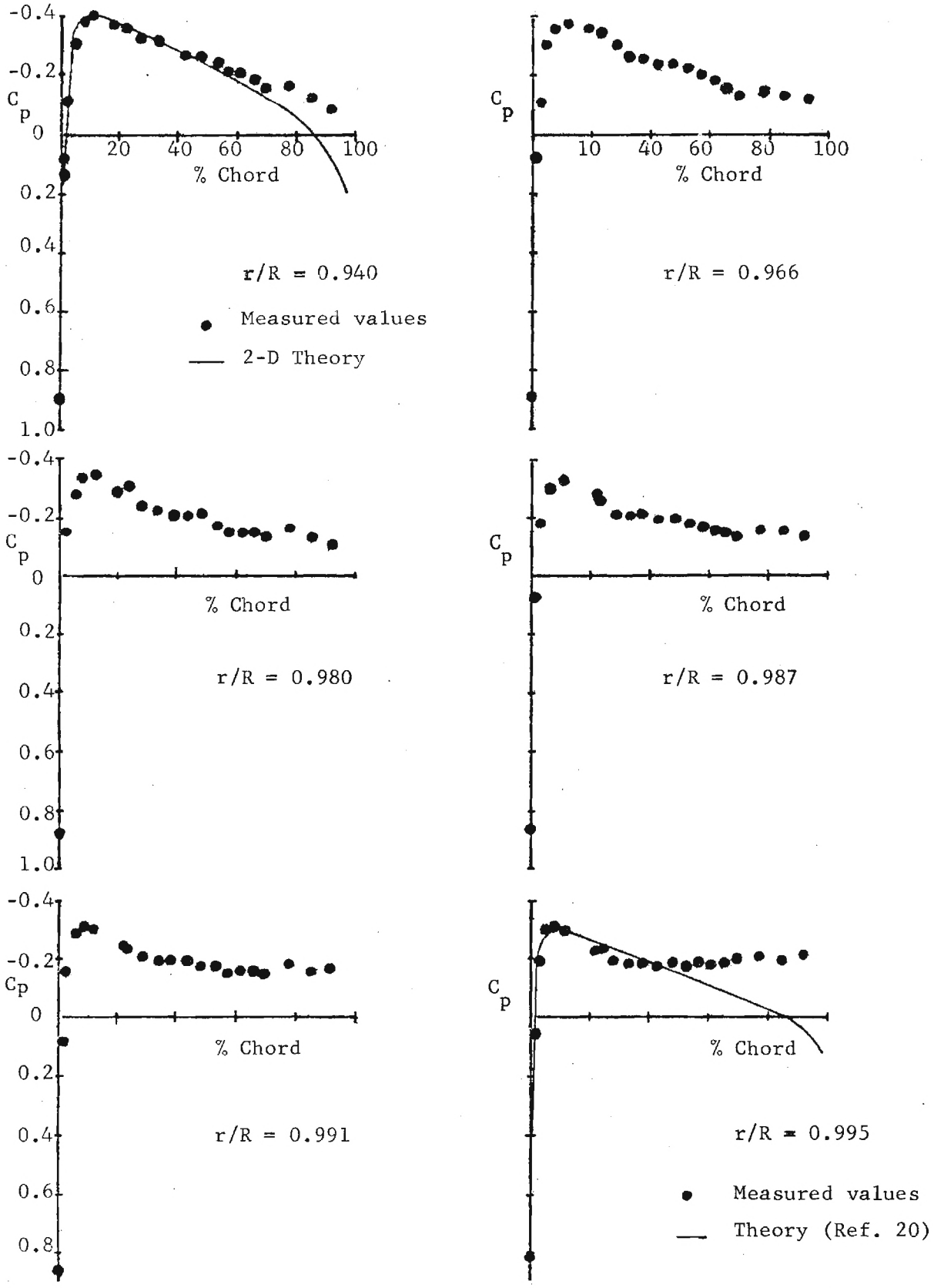

Figure 21. Pressure Distribution; $\theta=0^{\circ}$, RPM=1350

(r/R = 0.995) the agreement with the semi-infinite wing theory of Raj (Ref. 20) is good over the forward portion of the surface. At both stations the measured pressures are lower over the aft portions of the blade surface than those predicted by the theories. This difference is thought to be due to viscous effects and to a large radial velocity component (observed in flow visualization tests) which are not taken into account in the theories.

The pressure distributions at a pitch angle of 6.2° and 1350 RPM are plotted in Fig. 22. Again, the suction peak on the upper surface decreases as one proceeds toward the tip, while the pressure level on the lower surface increases slowly with increasing radius. At the innermost station (r/R = 0.94) the measured distribution is compared with that predicted by the rotor theory of Samant (Ref. 21) which takes account of inflow at the lifting line. It is seen that agreement is good over the forward portion of the section. Outboard of r/R = 0.987, there is a secondary suction pressure peak on the upper surface which is located at the 81% chord station ar r/R = 0.991 and which moves forward with increasing radius until it is at the 60% chord station at r/R - 0.995. This second peak is caused by the primary tip vortex (Fig. 23). Because of the higher pressure on the underside of the rotor, the flow is around the tip and onto the upper surface. A vortex is formed and coincident with its formation, local velocities are increased and surface static pressures are decreased in the areas described.

Figure 24 shows the pressure distribution on the surface of the square tip at 1350 RPM for pitch angles of 0° and 6.2°. The data are symmetrical about the rotor chord line at zero degrees. When the blade pitch angle is increased, the lower row of end pressure taps shows that a suction peak is established close to the leading edge and that there is a pressure decrease over the first 35% of the end of the blade when compared with the pressure on the adjacent lower surface of the blade. Along the blade chord (i.e., the middle row of pressure taps), the pressure has increased over the first 40% of the chord when compared with the pressures on the lower row while further aft along the chord a second suction peak is formed. This situation persists to the upper row of pressure taps and then between that row and the upper surface there is a further decrease in pressure over the front of the blade tip and a marked reduction in pressure around the 60% chord station where the vortex is formed.

Figure 25 shows a plot of lines of constant pressure on the upper surface of the rotor at 1350 RPM and 6.2°. The isobar pattern indicates that the tip vortex is centered at about the 60% chord station at r/R = 0.995 and moves inboard and aft. This was also shown in the movement of the second suction peak in the chordwise pressure distributions. The radial flow along the blade tip (from regions of high pressure to low pressure) is outboard over the first 45% of the surface, inboard from 45% to about 75%, and then outboard again. These changes in radial flow direction are due to the presence of the tip vortex on

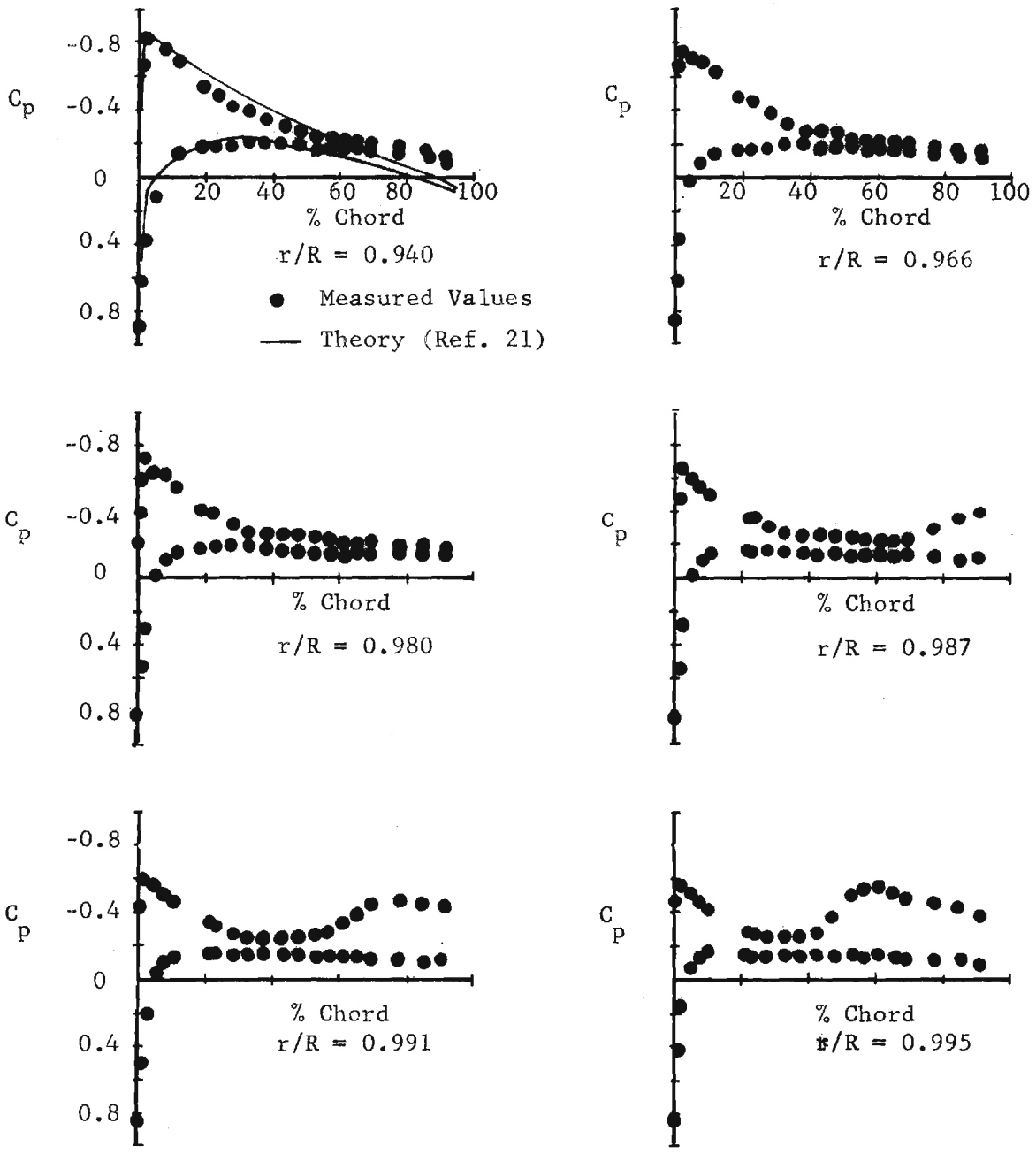

Figure 22. Pressure distribution; $\theta=6.2^{\circ}$, RPM=1350

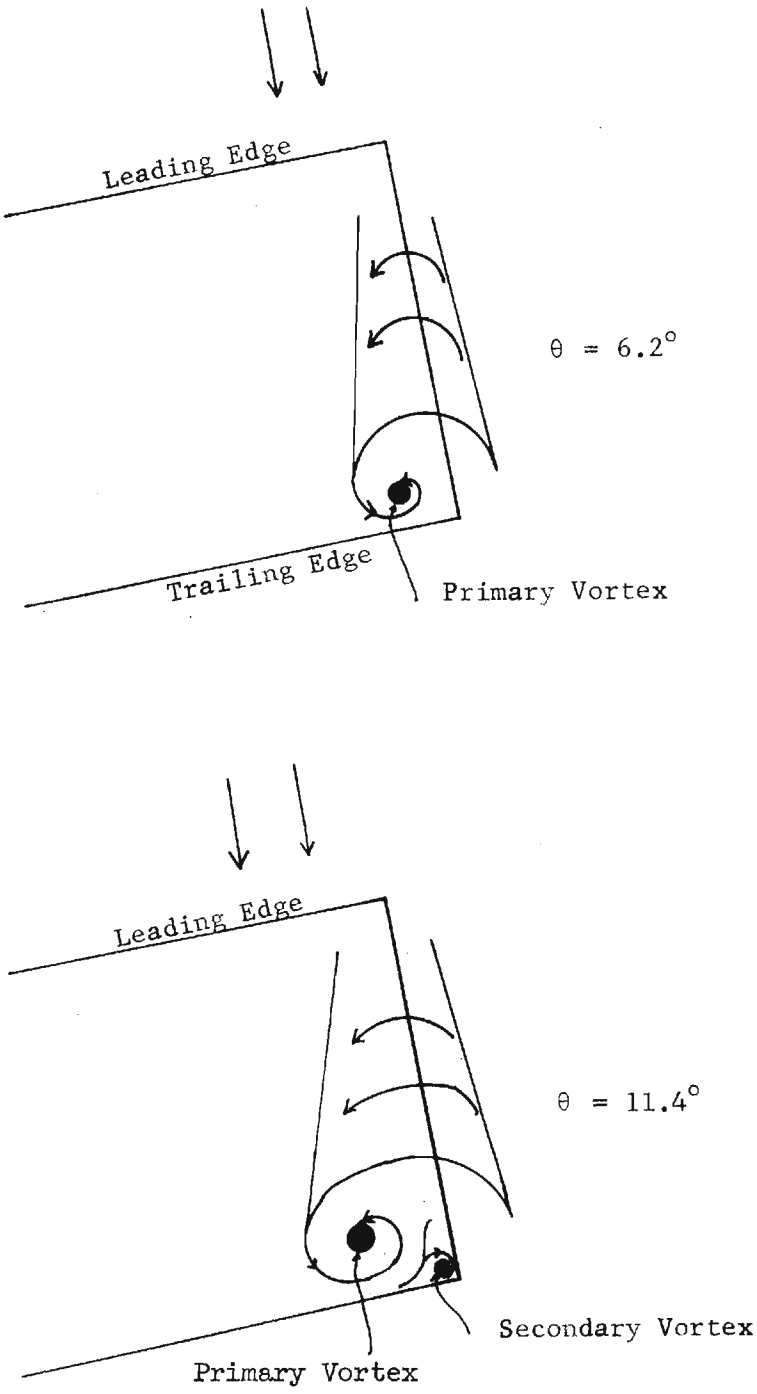

Figure 23. Formation of Tip Vortex

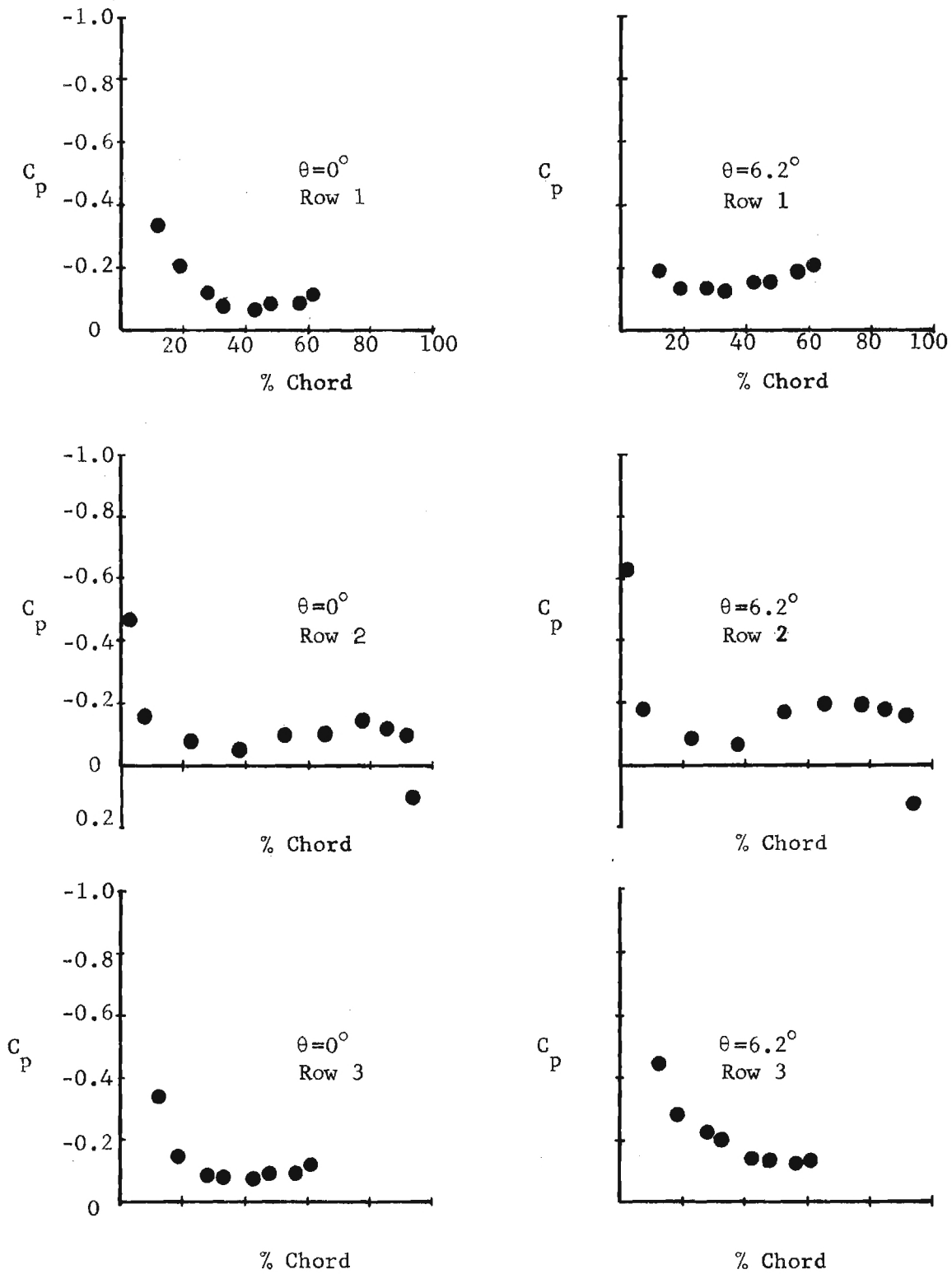

Figure 24. Pressure distribution on flat tip θ=0° and 6.2°; RPM=1350

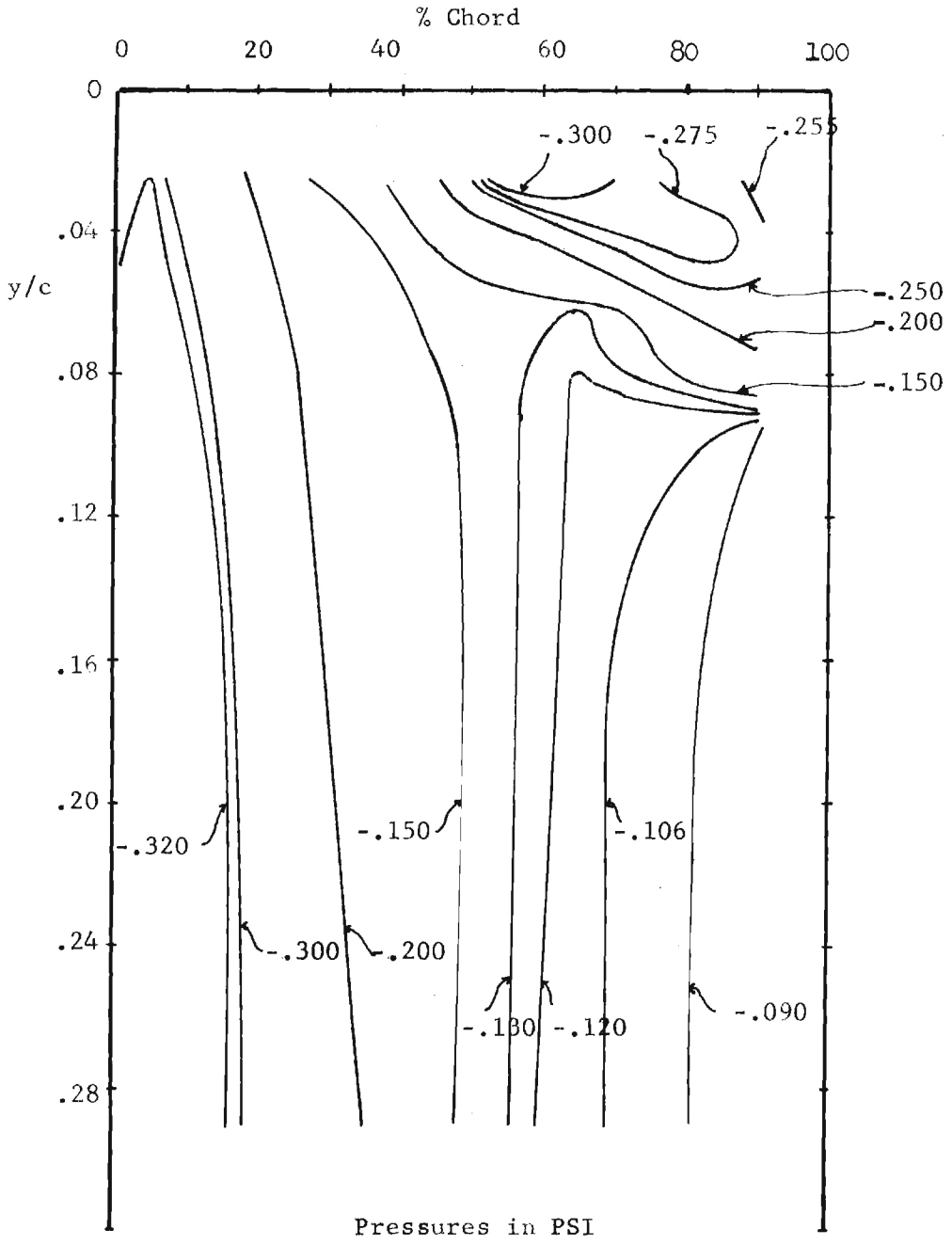

Figure 25. Isobars on the upper surface of rotor blade $\theta = 6.2^{\circ}$; RPM = 1350

the upper surface.

Figure 26 shows the chordwise pressure distribution on the upper surface near the tip at 1350 RPM and 11.4° pitch angle. Because of a short in the wiring inside the rotor blade there is a gap in the measurements where data from one cavity are missing. The expected phenomena, however, can be observed. At $r/R = 0.995$ there is seen to be a third suction peak not present (or significant) at 6.2°. This third suction peak is not observed at $r/R < 0.995$ at 11.4°. It is thought that a small secondary vortex located very near the tip and near the trailing edge (about 73% chord) is associated with this third peak. When these pressure distributions are compared with those for 6.2° of blade pitch angle, it is observed that the primary vortex moves toward the leading edge with increasing pitch angle.

The pressure data described in the preceding paragraphs were examined and the results compared with flow visualization studies (Ref. 12) made very near the tip of a rotor blade. The flow visualization techniques employed gave an indication of local flow direction and showed the presence of vortices on the upper surface of the rotor near the tip and also on the flat end of the blade. The surface flow direction inferred from the isobar plots (Fig. 25) agree well with the flow direction observed in Ref. 12. The point at which the radial flow direction suddenly changes near the tip was attributed in Ref. 12 to the inception of the tip vortex. The point of vortex inception from the pressure data (interpreted as the beginning of the second pressure decrease) compared well with that observed by flow visualization and the same trend was noted with increasing pitch angle. At 6.2° the present pressure data show the point of vortex inception to be at the 45% chord station whereas Ref. 12 indicates the 44% chord station. At 11.4°, the pressure data indicates vortex inception at the 29% chord station while Ref. 12 gives the 32% chord station.

The surface pressure measurements reported here were also compared with measurements made near the tip of a fixed wing (Refs. 17,18,19). The wing surface pressure measurements indicated the presence of a primary and secondary vortex near the tip at an angle of attack of 12 degrees. The same phenomena were observed in the present rotor tests at a pitch angle of 11.4°. However, in the case of the rotating blade the primary suction peak was further downstream than that measured for the fixed wing and the primary vortex is further outboard on the rotor than it is for the fixed wing.

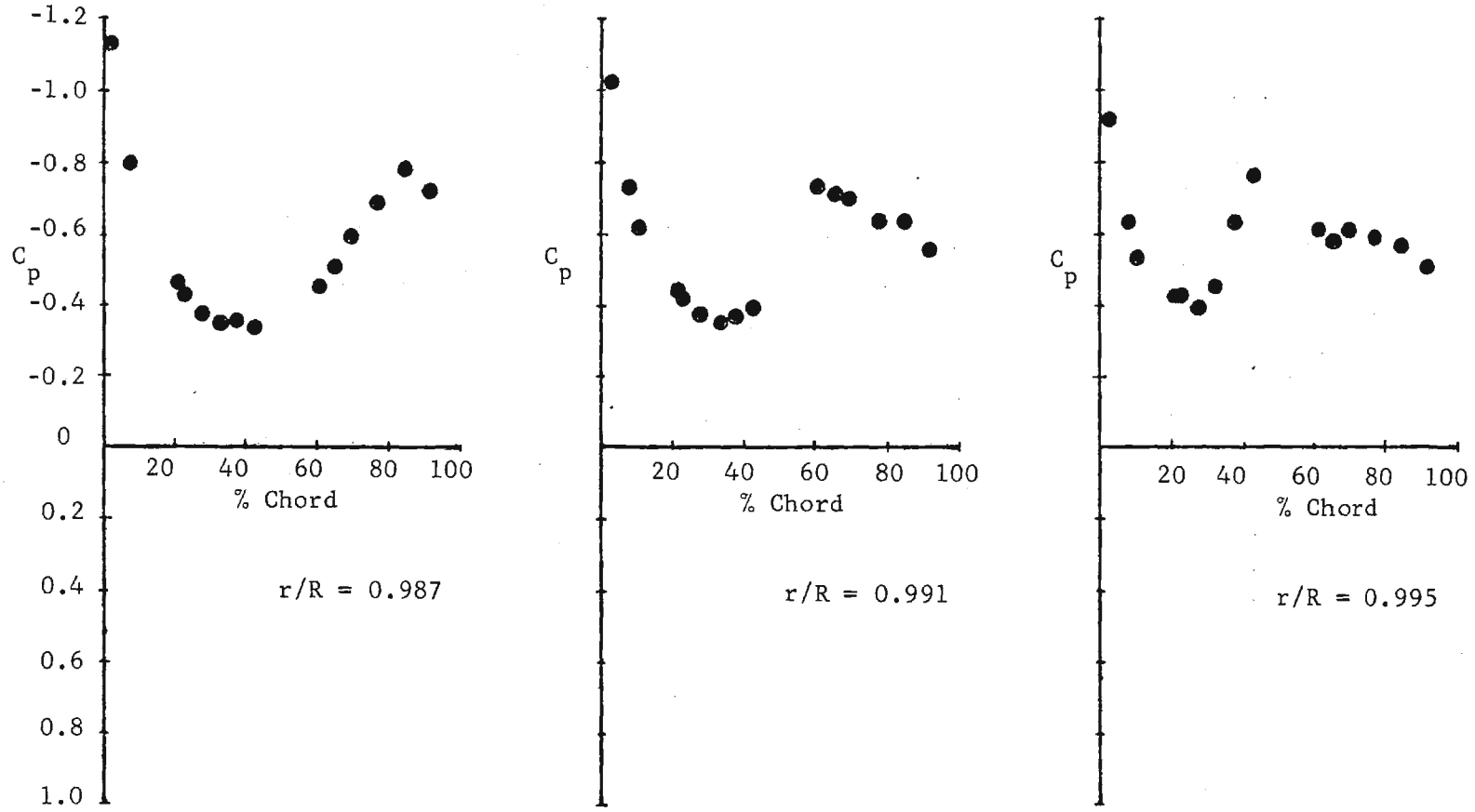

Figure 26. Pressure distribution on upper surface
$\theta = 11.4^{\circ}$; RPM = 1350

REFERENCES

1. Landgrebe, A. J. and Cheney, M. C., Jr., Rotor Wakes - Key to Performance Prediction, Symposium on Status of Testing and Modeling Techniques for V/STOL Aircraft, Mideast Region of the American Helicopter Society, Essington, Pa., Oct. 26-28, 1972. (Also, AGARD-CP-111, AGARD Conference Proceedings on Aerodynamics of Rotary Wings, Fluid Dynamics Specialists Meeting, Marseilles, France, Sept. 13-15, 1972).

2. Lock, C. N., Application of Goldstein's Airscrew Theory to Design, Aeronautical Research Committee (Great Britain), Report and Memorandum No. 1377, Nov. 1930.

3. Landgrebe, A. J., An Analytical and Experimental Investigation of Helicopter Rotor Hover Performance and Wake Geometry Characteristics, USAAMRDL Tech. Rep. 71-24, Eustis Directorate, U. S. Army Air Mobility Research and Development Laboratory, Ft. Eustis, Va., June 1971.

4. Gray, R. B. and Brown, G. W., A Vortex-Wake Analysis of a Single-Bladed Hovering Rotor and a Comparison with Experimental Data, AGARD-CP-111, AGARD Conference Proceedings on Aerodynamics of Rotary Wings, Fluid Dynamics Panel Specialists Meeting, Marseilles, France, Sept. 13-15, 1972.

5. Landgrebe, A. J. and Egolf, T. A., Prediction of Helicopter Induced Flow Velocities Using the Rotorcraft Wake Analysis, 32nd Annual National V/STOL Forum of the American Helicopter Society, Preprint No. 1002, Washington, D. C., May 1976.

6. Gray, R. B., On the Motion of the Helical Vortex Shed from a Single-Bladed Hovering Helicopter Rotor and Its Application to the Calculation of the Spanwise Aerodynamic Loading, Princeton University Aeronautical Engineering Department, Report No. 313, Sept. 1955.

7. Gray, R. B., An Aerodynamic Analysis of a Single-Bladed Rotor in Hovering and Low-Speed Forward Flight as Determined from Smoke Studies of the Vorticity Distribution in the Wake, Princeton University Aeronautical Engineering Department, Report No. 356, Sept. 1956.

8. Kocurek, J. D. and Tangler, J. L., A Prescribed Wake Lifting Surface Hover Performance Analysis, 32nd Annual National V/STOL Forum of the American Helicopter Society, Preprint No. 1001, Washington, D. C., May 1976.

9. Hoerner, S. F., Fluid-Dynamic Drag, Published by the Author, 1965.

10. Jacobs, E. N. and Sherman, A., Airfoil Section Characteristics as Affected by Variations of the Reynolds Number, NACA TR 586, 1937.

11. Bailey, F. J., Jr., A Simplified Theoretical Method of Determining the Characteristics of a Lifting Rotor in Forward Flight, NACA TR 716, 1941.

12. Hoffman, J. D. and Velkoff, H. R., Vortex Flow Over Helicopter Rotor Tips, AIAA Journal of Aircraft, Vol. 8, September 1971, pp. 739-740.

13. Scheimann, J. and Ludi, L. H., Qualitative Evaluation of Effect of Helicopter Rotor Blade Tip Vortex on Blade Airloads, NASA TND-1637, May 1963.

14. McCormick, B. W. and Surendraiah, M., A Study of Rotor Blade-Vortex Interaction, 26th Annual National Forum of the American Helicopter Society, Washington, D.C., June 1970.

15. White, R. P. and Balcerk, J. C., The Nemesis of the Trailed Tip Vortex - Is It Now Conquered? 28th Annual National Forum of the American Helicopter Society, Washington, D. C., May 1972.

16. Spivey, W. A. and Morehouse, G.A., New Insights into Design of Swept-tip Rotors, 26th Annual National Forum of the American Helicopter Society, Washington, D.C., June 1970.

17. Spivey, R. F., Blade Tip Aerodynamics - Profile and Planform Effects, 24th Annual National Forum of the American Helicopter Society, Washington, D.C., May 1968.

18. Chigier, N. A., Experimental Studies of Turbulent Aircraft Wakes, Israel Journal of Technology, Vol. II, 1973, pp. 367-372.

19. Chigier, N. A. and Corriglia, V. R., Tip Vortices-Velocity Distributions, 27th Annual National Forum of the American Helicopter Society, Washington, D. C.,May 1971.

20. Raj, P., A Method of Computing the Potential Flow on Thick Wing Tips, School of Aerospace Engineering, Georgia Institute of Technology, Ph.D. Dissertation to be published.

21. Samant , S., An Improved Method for Calculating the Tip Vortex Geometry for Hovering Rotors, School of Aerospace Engineering, Georgia Institute of Technology, Ph.D. Dissertation to be published.

GLOSSARY

A	wake contraction ratio
b	number of blades
c	blade chord
C	wake geometric parameter, $1 - A$
C_Γ	tip vortex strength coefficient, $\Gamma/4\pi\Omega(RA)^2$
C_Q	rotor torque coefficient, $Q/\rho\pi\Omega^2R^5$
C_p	blade pressure coefficient, $2(p - p_\infty)/\rho\Omega^2r_p^2$
C_T	rotor thrust coefficient, $T/\rho\pi\Omega^2R^4$
D	diameter
i	exponent: 1, 0, -1
J	tip vortex strength parameter
K_1	geometric parameter defining axial position of tip vortex in near wake
K_2	geometric parameter defining axial position of tip vortex beyond near wake
Q	rotor torque
p	blade surface pressure
p_∞	ambient pressure
r	radial location on rotor blade
r_p	radius of point p
R	rotor tip radius
T	rotor thrust
u_{a_p}	nondimensional apparent radial induced velocity, $u'_{a_p}/\Omega RAC_\Gamma$

u'_{a_p} apparent radial induced velocity at point p associated with entire vortex system including the tip vortex core

u_p nondimensional radial induced velocity, $u'_p/\Omega RAC_\Gamma$

u'_p induced radial velocity at point p associated with entire vortex system except the tip vortex core

v_c nondimensional induced tangential velocity associated with the tip vortex core, $v'_c/\Omega RAC_\Gamma$

v'_c induced tangential velocity associated with the tip vortex core

v_p nondimensional tangential induced velocity, $v'_p/\Omega RAC_\Gamma$

v'_p induced tangential velocity at point p associated with entire vortex system except the tip vortex core

w_{a_p} nondimensional apparent axial induced velocity, $w'_{ap}/\Omega RAC_\Gamma$

w'_{a_p} apparent axial induced velocity at point p associated with entire vortex system including the tip vortex core

w_p nondimensional axial induced velocity, $w'_p/\Omega RAC_\Gamma$

w'_p induced axial velocity at point p associated with entire vortex system including the tip vortex core

x_p nondimensional radius of point p , r_p/RA

y distance inboard from rotor tip

Greek Letters

β_p radial pitch angle of tip vortex at point p

Γ tip vortex strength

θ blade pitch angle

λ measured parameter defining rate of contraction of wake

ρ air density

σ	blade solidity, $bc/\pi R$
φ_p	axial pitch angle of tip vortex at point p
Ψ	azimuth angle from blade to point p
Ω	rotor angular velocity